Materials & Design 260 (2025) 115252

Contents lists available at ScienceDirect

Materials & Design

journal homepage: www.elsevier.com/locate/matdes

Satellite-free droplet formation in material jetting via rheology-driven waveform modelling approach

Karin J. Chen [a,b,*], Veit Hagenmeyer [a], Ahmed Elkaseer [c]

[a] Institute for Automation and Applied Informatics, Karlsruhe Institute of Technology, Hermann-von-Helmholtz-Platz 1, Eggenstein-Leopoldshafen 76344, Germany
[b] Karlsruhe Nano Micro Facility, Karlsruhe Institute of Technology, Hermann-von-Helmholtz-Platz 1, Eggenstein-Leopoldshafen 76344, Germany
[c] Department of Mechanical Engineering, Faculty of Engineering, The British University in Egypt, El-Sherouk City 11837, Egypt

ARTICLE INFO

Keywords:
Material Jetting
3D inkjet printing
Viscoelastic non-Newtonian polymer Inks
Rheology–driven waveform optimisation
Satellite-free droplet formation
Regression modelling

ABSTRACT

Stable, satellite-free droplet ejection is essential for high-resolution material jetting (also known as 3D inkjet printing). Existing "printability windows" often fail to predict satellite formation accurately, as they neglect non-Newtonian fluid behaviour and waveform dynamics. This study presents a fast-track, experiment-driven approach to identify single-droplet waveform parameters, namely pulse width and driving voltage, from rheological data of polymer inks across different jetting temperatures, eliminating tedious drop-watching trials. Three UV-curable acrylate inks are systematically characterized for complex viscosity, viscoelasticity, relaxation time, dynamic surface tension, oscillation and damping behaviour, and density at five temperatures using a high-frequency squeeze-flow rheometer and bubble tensiometer. Cross, Hua & Rosen, Maxwell, Arrhenius, and Eötvös models are applied to extrapolate these properties to the inkjet regime ($\sim 10^5$ s^{-1} shear rate, <1 ms surface age). A correlation between droplet velocity and driving voltage, dependent on material properties, is established. Satellite formation is governed almost exclusively by droplet velocity, with distinct regimes: <3 m/s (no satellite), 3–3.8 m/s (one satellite). A general equation quantifying the relationship between droplet velocity and driving voltage enables predictive waveform design from rheological data. The methodology, validated with two UV-curable inkjet inks, accelerates the search for a satellite-free single droplet waveform.

1. Introduction

Material Jetting (MJ), also known as 3D inkjet printing (3D-IJP), is an additive manufacturing process that employs piezo-based inkjet technology to build three-dimensional objects. A typical printhead contains thousands of nozzles, each lined with piezoelectric actuators. When driven by a programmed electrical signal, termed waveform, these actuators deform and fire a droplet from the nozzle every time a signal is applied.

Objects are formed layer by layer by ejecting and rapidly solidifying arrays of micron-scale droplets by UV-curing [1]. As the droplets coalesce, they define the cross-sectional pattern of the 3D model. The minute droplet size affords MJ exceptionally high dimensional accuracy and fine feature resolution, giving it distinct advantages over most other commercial additive manufacturing technologies. Furthermore, by installing multiple printheads in the printer, multi-colour printing can simply be facilitated. With MJ, applications such as dental implant [2], printed photodiodes [3], tissue-mimicking medical models [4] and soft robots [5] have been explored. Inkjet printing is also increasingly used in advanced manufacturing of semiconductor, optoelectronic or electronic application, including transistors [6,7], photodiode [3], optical interference filters [8] and antenna [9].

Droplet formation in inkjet printing is governed by multiple interacting forces, namely inertia, surface tension, viscous force, and elastic force (Fig. 1). In the initial stage of jetting, inertia and surface tension play dominant roles, whereas during the droplet-in-flight phase, the jetting itself is restricted by the shear viscosity [10,11]. During the ejection process, viscosity recovers from the high shear rate within approximately 100 μs [12]. In the intermediate phase, viscoelastic properties dominate [10,11]. In the final phase, that is the detachment of the droplet from the nozzle, extensional viscosity becomes the governing parameter [10,11,13]. The exit velocity at nozzle appears to be governed solely by the infinite shear viscosity, while drop velocity depends on the extensional viscosity [11].

Fig. 1 visualizes the interplaying forces during the droplet formation

* Corresponding author at: Institute for Automation and Applied Informatics, Karlsruhe Institute of Technology, Hermann-von-Helmholtz-Platz 1, Eggenstein-Leopoldshafen 76344, Germany.
E-mail address: karin.chen@kit.edu (K.J. Chen).

https://doi.org/10.1016/j.matdes.2025.115252
Received 24 July 2025; Received in revised form 26 October 2025; Accepted 1 December 2025
Available online 2 December 2025

Nomenclature

Variables

A	Pre-exponential factor (Arrhenius model)
C	Constant (Cross model)
E_{stor}	Elastic coefficient of fitted storage modulus (Maxwell model)
E_{loss}	Elastic coefficient of fitted loss modulus (Maxwell model)
E_a	Activation energy (Arrhenius model)
f	Frequency, Hz
G'	Storage modulus
G''	Loss modulus
k	Eötvos constant (Eötvös model)
l_{PH}	Travel length in printhead (nozzle channel length)
l_{rheo}	Travel length in squeeze-flow rheometer (diameter)
m	Slope coefficient (linear equation)
N_{sat}	Number of satellite droplets
p	Pressure
q	Y-intersect constant (regression model)
r	Bubble radius
R	Gas constant
s	Fit parameter (Hua & Rosen model)
T	Temperature
t	Time
T_c	Critical temperature (Eötvös model)
$t_{osc,p}$	Time of peak (oscillation measurement)
$t_{osc,t}$	Time of trough (oscillation measurement)
$t_{PW,opt}$	Optimal pulse width
t_{PW}	Pulse width
$U_{osc,in}$	Input voltage (oscillation measurement)
$U_{osc,out}$	Output voltage (oscillation measurement)
$U_{osc,p}$	Output voltage of peak (oscillation measurement)
$U_{osc,t}$	Output voltage of trough (oscillation measurement)
$V(H)$	Driving voltage in waveform for high pulse section
V_d	Droplet volume
$V_{d,dw}$	Droplet volume according to dropwatcher
$V_{d,w}$	Droplet volume according to weight test
V_M	Molar volume (Eötvös model)
$V_{rel}(H)$	Relative driving voltage to EEPROM value, printhead-specific
v	Droplet velocity
$\alpha_{1,q}$	Scalar coefficients for complex viscosity (linear regression, y-intersect)
$\alpha_{2,q}$	Scalar coefficients for surface tension (linear regression, y-intersect)
$\alpha_{3,q}$	Scalar coefficients for density (linear regression, y-intersect)
$\alpha_{4,q}$	Scalar coefficients for storage modulus (linear regression, y-intersect)
$\alpha_{1,m}$	Scalar coefficients for complex viscosity (linear regression, slope)
$\alpha_{2,m}$	Scalar coefficients for surface tension (linear regression, slope)
$\alpha_{3,m}$	Scalar coefficients for density (linear regression, slope)
$\alpha_{4,m}$	Scalar coefficients for storage modulus (linear regression, slope)
$\dot{\gamma}$	Shear rate
η^*	Complex viscosity
λ	Relaxation time
ρ	Density
σ	Surface tension
τ	Characteristic time (Hua & Rosen model)
ω	Angular frequency

Subscript symbols

MJ	Material Jetting
Avg	Average
M1/2/3	Material 1,2,3
PH0/1	Printhead 0 and 1
St. Dev	Standard deviation

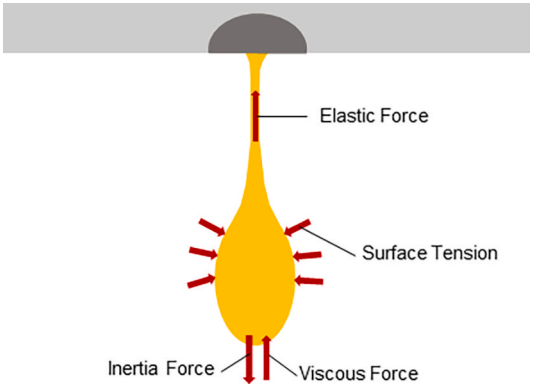

Fig. 1. Governing forces in the droplet formation process in inkjet printing

in inkjet printing. Surface tension plays a key role in thinning the liquid ligament, in pinching off droplets from the nozzle and in breaking up the liquid filament into spherical droplets, the shape with the lowest surface energy [14]. Inertia and viscous force oppose the contraction of the liquid filament driven by surface tension [15]. Strong elastic force hinders droplet detachment from the printhead, but can also suppress the formation of satellite droplets by holding the liquid molecules together [13]. In addition to the ink's physical properties, the obtained droplet shape and behaviour during jetting are also influenced by the actuating signal [16,17] and the specific architecture of the printhead.

An optimal jetting condition is achieved if the nozzles of the printhead jet one single droplet for each pulse with a consistent speed, steady volume and with a straight trajectory [18]. However, in some cases, the jetted liquid disintegrates into multiple sub-droplets while travelling to the substrate. These sub-droplets are also known as satellite droplets. If these satellite droplets do not merge with the head droplet within the print distance, small droplets will be printed outside the print area which not only reduce the fidelity of the geometry but also compromise the functionality of the printed part.

Wijshoff (2008) named several jetting scenarios that lead to the formation of satellite droplets [19]. First, satellite droplets occur when the length of the tail of the jetted droplet exceeds the critical length $L_{critical}$. Beyond this length, the existing periodic disturbance of the liquid column becomes unstable and the amplitude of the perturbation increases, resulting in necking of the liquid column. Eventually the liquid column splits up into several small spherical droplets as this geometry is energetically more favorable. This phenomenon is first described by Rayleigh in 1878 [20] and is known as Rayleigh instability. Eq. (1) describes the critical length for the onset of satellite drops for an inviscid material [21].

$$L_{critical} \sim \left(\frac{\rho v^2 R^3}{\sigma}\right)^{1/2} \tag{1}$$

If velocity, density and radius of the jet are higher, the liquid column can be longer without the onset of instability, whereas an increased surface

tension leads to instability for even shorter liquid column (Eq. (1)). Similarly, for a fixed print distance, a jetted liquid tail will not disintegrate into satellite drops if the velocity is below a certain level.

Khodayari et al. modelled the liquid jet break-up behaviour for non-Newtonian viscoelastic liquid [22]. The findings indicate that increased viscosity enhances the dissipation of disturbance, thus the breakup length raises, whereas a greater elasticity amplifies the instability and leads to a shorter breakup length [23]. Other study reports that some materials are more prone to satellite drops because of the strain-hardening effect of the material due to stretching. The material property relaxation time is relevant to gauge this behaviour [24].

Another jetting behaviour that leads to satellite droplets is excessive jetting speed, which makes the head droplet detach from the rest of the droplet while in motion [19]. Further, in a draw-reinforce-release waveform, the pulse widths for each regime are interrelated and a greater-than-optimal pulse width might lead to two positive pressure waves to be generated in one pulse. As a result, one main droplet and one satellite droplet are being jetted [19]. In both scenarios, a suboptimal pulse width is reported to be the cause. The optimum pulse width corresponds to the time duration at which droplet velocity is maximized, and this value depends on the channel geometry and the acoustic speed of the material [25].

In order to prevent satellite droplets induced by Rayleigh instability, the tails of the droplets are to be shortened or eliminated. By reducing the flow rate of the ink through the nozzle, the liquid ligament breaks off around the nozzle which reduces the length of the tail considerably. The flow rate is directly related to the driving waveform such as driving voltage. Several studies observed that when jetting velocity exceeds a certain threshold, typically due to increased driving voltage, satellite droplets emerge [26–28].

Several studies investigated the correlation between waveform and droplet formation. With the relationship being quadratic, any pulse widths shorter or longer than the optimum value result in the droplet velocity to drop [29]. Driving voltage and droplet velocity are correlated in a positive linear manner, a dependency present across several different printhead types [30,31]. However, an increased voltage can lead to the formation of a longer ligament, which is more likely to disintegrate into multiple satellite droplets. For an ink with elastic properties, the minimum driving voltage becomes higher as more kinetic energy is required to overcome the surface tension of the meniscus at the nozzle and to eject droplets [32]. Complex waveforms are designed to reduce the emergence of satellite droplets [27] and to control the jetting velocity [33] of the resulting droplet.

Meanwhile, numerous studies also investigated the relationship between the ink's rheological properties and the droplet behaviour [34,35]. Morrison et al. (2010) observed that the number of satellite droplets is correlated with the concentration and molecular weight of the polymeric fluid [36]. Tuladhar et al. (2009) observed that for an ink with elasticity value less than 10 %, defined as the ratio of the storage modulus (G') to the complex modulus (G*), satellite-free droplets can be generated [37]. Sen et al. (2021) found that the storage modulus (G') should remain low during jetting, but in flight, a high G' value is favourable for maintaining a single droplet and preventing the formation of satellite droplets [38].

The most common approach to assess whether a material is jettable or not is by utilizing dimensionless numbers that represent the ratio between material properties. For instances, Derby et al.'s (2010) operating window proposes that materials with Ohnesorge number (Oh) between 0.1 and 1 enable droplets without satellite droplets [39,40]. Liu et al. (2019) and Jang et al. (2009) extended the study with more inks to update Oh [25,35]. Some studies attempt to include other properties to predict a print window, e.g., by plotting Weber number (We) and the inverse of Oh [35,41], Oh over Reynolds number (Re) [42,43], or Capillary number (Ca) over We [44,45].

Garcia-Tunon et al. (2023) propose a new approach based on the rheological measurement of G' and loss modulus G''. The map indicating the printability area features G' over the cross-over point of G' and G'' [46]. For non-Newtonian ink, one study mapped Deborah number (De) over the meniscus displacement to correlate to the printhead driving settings [38]. Material with Weissenberg number $Wi = 0.5$ produces a single and stable droplet [47]. Further studies suggest to look into De and Oh [48], Re and Ca [49], or De and We [50] to predict the jettability of viscoelastic droplets.

However, it has been observed that in practice, even when an ink meets the above-mentioned printability criteria, stable jetting of a single satellite-free droplet is not guaranteed. Time-consuming experimental studies deploying a dropwatcher remain necessary to determine a waveform capable of producing stable droplets. This discrepancy between theoretical predictions and practical outcomes arises from several factors:

First, some of these printability windows were derived based on simulation studies and assumed Newtonian fluid behaviour. Polymer-based inks very often exhibit non-Newtonian fluid behaviour [51,52], such as shear-thinning, and show viscoelasticity. Both characteristics typically emerge at higher shear rates [53] and the shear rates at the printhead nozzle channels are approximately $10^5 s^{-1}$ to $10^6 s^{-1}$ [54]. Further, previous studies assess the printability based on properties obtained at a static dynamic range. For inkjet printing, it is advisable to consider the materials' properties at higher dynamic range which only few measurement devices can assess [55,56].

Furthermore, existing fast-track approaches exclude the role of waveform. Fig. 2 visualizes the droplet behaviour of one material assessed on a dropwatcher at 26 °C, located in the We/Re-plot according to Derby et al. [39]. This printable window is commonly deployed by numerous studies to gauge whether an ink is printable or not [47,57,58]. The thresholds for satellite droplets and high-viscous material jetting are defined by the Z number, inverse of Oh, which is defined as $Z = \frac{\sqrt{\rho\sigma d}}{\eta} = \frac{\sqrt{(We)}}{Re}$, with ρ, σ, d and η being density, surface tension, diameter of the droplet and viscosity, respectively. By increasing the driving voltage, the number of satellite droplets (see colour of the data points) increased, despite the material properties remain the same. Both We and Re increase when the driving voltage is raised, because the jetting velocity increases linearly. As a result, the data points shift parallel to the satellite droplet threshold, moving toward the splashing threshold. Even outside the printable regime, a suitable driving voltage can achieve single droplet printing. The plotted data also reveal variability among nozzles (each marker geometry corresponds to a specific nozzle). Overall, the We/Re-plot is not sufficient to determine the jettability of an ink.

Few studies attempt to include printhead-related specifications to define the jettability. Bazilevskii et al. (2005) consider the jet diameter, mass of droplet, elastic modulus and extensional relaxation time for predicting the droplet detachment process [59]. Zhao et al. (2021) deploy a dimensionless number W_j that takes into account the aspect ratio of the ligament, the mean droplet velocity and the diameter of the nozzle, and the pulse-width of the driving waveform [60]. Götz et al. (2025) propose a comparative approach: matching the rheological properties of commercial inks with those of a set of basic inks for which potential waveforms are already known. Depending on the properties of the commercial ink, it is assumed that a waveform from a similarly behaving basic ink can then be selected [61].

Based on the presented studies, it can be inferred that existing approaches for determining a stable printable range with single droplet jetting ex-situ are insufficient as they fail to account for several major findings:

(1) Polymer inkjet inks behave in a non-Newtonian way and thus, properties related to viscoelasticity should be regarded.
(2) Material properties of non-Newtonian ink in high dynamic range (high shear rate, short time scale) deviate from the static range.

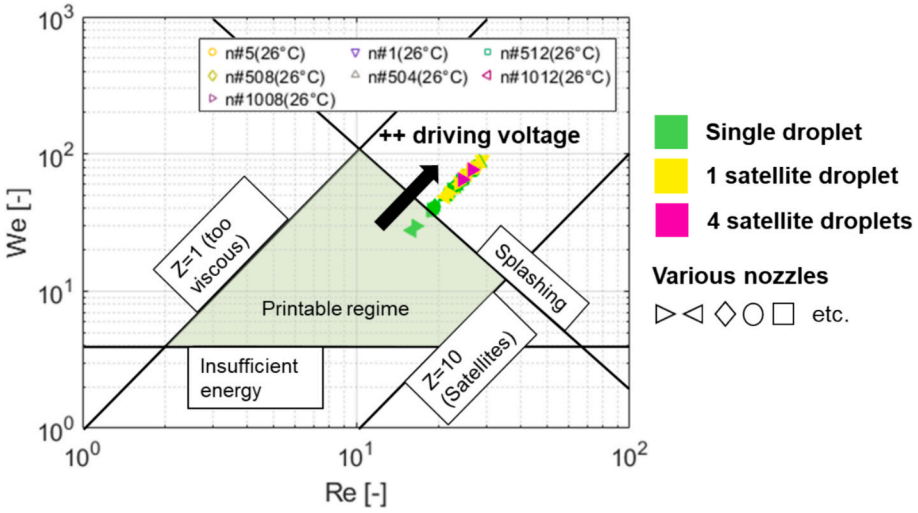

Fig. 2. The variability of drop formation by modifying driving voltage

To understand the jetting behaviour, material properties at high dynamic range should be considered.

(3) 3D inkjet printing requires a complex formulation of ink and very often, existing models in material science are only applicable to homogeneous material. Therefore, the criteria for assessing jettability should consider bulk properties such as viscosity and surface tension, and not molecular-level properties such as chain length, molecule concentration, etc., as these characteristics are difficult to determine if multiple components are involved in the formulation of the ink.

(4) The formation of satellite droplets is correlated with jetting velocity, as governed by Plateau-Rayleigh instability. Since each printhead's geometry and waveform representation differs, the jetting velocity can serve as a universal target criterion.

(5) Jetting velocity is correlated to driving voltage in a linear manner

(6) Jetting velocity depends on the properties of the viscoelastic ink, since the energy transfer varies even under identical kinetic energy input. The relevant material properties according to literature are shear complex viscosity, surface tension, density, storage modulus and relaxation time.

(7) The optimum pulse width is mainly related to the printhead architecture and material's acoustic property.

The objective of this study is to develop a simple, robust and practical methodology for determining a unipolar waveform that enables stable single-droplet across a range of jetting temperatures while addressing the gaps identified in previous studies and outlined above. This methodology is the first of its kind, as it relies exclusively on experimentally accessible and literature-relevant rheological and physical properties. The approach should leverage the correlation between jetting velocity and satellite droplet formation.

First, the materials applied in this study including the models to extend the measured properties to the relevant dynamic range and temperatures in inkjet printing are introduced. These results are then synthesized and correlated with the dropwatching results, and a regression curve is proposed which links the ink's physical properties with the waveform driving parameters and the droplet formation behaviour. The bipolar waveform will be generated in two steps – first, the optimum pulse width is determined, second, the driving voltage is adjusted to control the droplet formation. The approach will be validated with a third material. In the Conclusion Section suggestions for future studies can be found.

2. Materials and methods

2.1. Inkjet materials

Two acrylate-based UV-curable inks from the company Notion Systems ("noptics", named "M1" in this study) and Altana ("S5000", named "M2") are deployed for deriving the methodology. M1 comprises of isobornyl acrylate while M2 is based on acrylate monomers and polyethylene glycol. Material "M3" from Altana ("1200 Clear") is deployed for validation and contains acrylate monomers as well.

2.2. Characterization

2.2.1. Density

Densities from 25 °C to 50 °C are measured on the densimeter by Anton Paar (DMA 4100 M). The densimeter oscillates the U-shaped tube filled with the material and determines the density based on the difference in frequency between a loaded and unloaded tube [62].

2.2.2. Complex viscosity and viscoelasticity

Complex viscosity η^* and viscoelastic properties expressed as storage G' and loss modulus G'' are measured with the squeeze-flow rheometer TriPAV by Trijet. The squeeze-flow rheometer oscillates the ink placed between two plates by utilizing the piezo elements attached to the lower plate. The oscillation squeezes the material between the plates over a wide range of frequencies and the resulting movement of the material is translated into an output voltage of the piezo actuator which allows the complex viscosity and viscoelastic moduli to be derived [55].

The characterization of the materials M1, M2 and M3 is carried out through the following steps: First, the actual shim size at a particular temperature is determined by using standard viscosity fluid N10 by VWR Chemicals. The calibration is conducted at temperatures 25 °C, 37.78 °C and 40 °C as the reference viscosities of the standard viscosity fluid are only given at these temperatures. For any other temperatures within 25 °C and 40 °C, the corresponding shim sizes are determined by linear interpolation. The calibration is conducted for both shim thicknesses 10 μm (sh10) and 20 μm (sh20).

Second, the measurement of the ink is conducted at the temperature settings given in Table 1, namely at 26 °C, 28 °C, 30 °C, 35 °C for material M1, and 25 °C, 37.8 °C for material M2. The measurement is performed within a temperature tolerance range of $\pm 0.3^{\circ}C$. The number of measurement points is set to 150, logarithmic spacing, for the frequency range 1 Hz to 10^4 Hz. The measurement requires a liquid volume of 150 μl which is applied with a micropipette (Eppendorf Research®

Table 1
Waveform parameters range applied to M1 and M2. $t_{PW}(H)$ is the pulse width of the high pulse, $V(H)$ is the driving voltage of the high pulse section, $V_{rel}(H)$ is the relative driving voltage with respect to the EEPROM value $V(H)_{EEPROM}$, a value specific for each printhead (Printhead 0 (PH0): 11.9 V, Printhead 1(PH1): 12.2 V). $V(L)$ is half of $V(H)$. T is the jetting temperature.

Material	T	t_{Pw}(H)	V(H)	V_{rel}(H)
[–]	[°C]	[μs]	[V]	[%]
M1 (noptics)	26 °C/28 °C/30 °C/35 °C	6–8	7.65–12	63–82
M2 (Altana S5000)	25 °C/37.8 °C	6–8	9.5–13.09	78–110

plus 20–200 μl).

Two shim sizes, 10 and 20 μm, are required to measure the complex viscosity over the entire frequency range. The sensitivity of the measured signal depends largely on the gap size between the upper and lower plate. For lower frequency range a bigger gap size is to be used, whereas for higher frequency a smaller shim size is required.

The measured data are cleaned in two steps before being joint together. First, data points with sensitivity larger than value 1 are omitted as it implies that the noise of the device exceeds the measured signal. Second, the data measured with each shim size are further truncated. In particular, the complex viscosity values obtained with sh10 is truncated for frequencies greater than the cutoff frequency ($f > f_{cutoff}$), whereas the values measured with sh20 are removed before the cutoff frequency ($f < f_{cutoff}$). The cutoff frequency is the value at which both measured complex viscosities differ least. The loss and storage modulus data are trimmed based on the same cutoff frequency.

According to Cox-Merz rule [63], the complex viscosity from oscillatory measurement is approximately equal to steady shear viscosity. For example, the complex viscosity obtained at 10^4 Hz oscillatory frequency is roughly the shear viscosity at 62832 s^{-1} shear rate.

2.2.3. Surface tension

Dynamic surface tensions are measured with a maximum bubble tensiometer (SITA pro line t15+, SITA Messtechnik). The bubble tensiometer utilizes the relationship between bubble radius, surface tension and bubble pressure, the so called Laplace-Equation (Eq. (A.1), Appendix) [64] and measures the pressure for bubbles generated within different time periods, controlled by the flow rate of the gas inlet [65]. Surface age sweep from 15 ms to 2000 ms is conducted during the measurement. Each material is measured at the temperatures as given in Table 1, with a temperature tolerance range of $\pm 1K$. The obtained value represents the averaging of 10 measurements.

2.2.4. Oscillation and damping behaviour

The squeeze-flow rheometer operated with an oscilloscope emulates the piezo displacement in a printhead. The gap size selected for this measurement should be similar to the printhead channel size to mimic the printhead channel condition. Since the exact nozzle channel size of the printhead is unknown, an estimation is made based on the nominal droplet volume. The printhead's nominal droplet volume is 30 pl, which is equivalent to a droplet diameter of 38.4 μm. Assuming that the nozzle channel width is at least the diameter of the nozzle, a shim size of 50 μm is used for this measurement. Fig. 3 gives an overview of the materials and methodology deployed in this study.

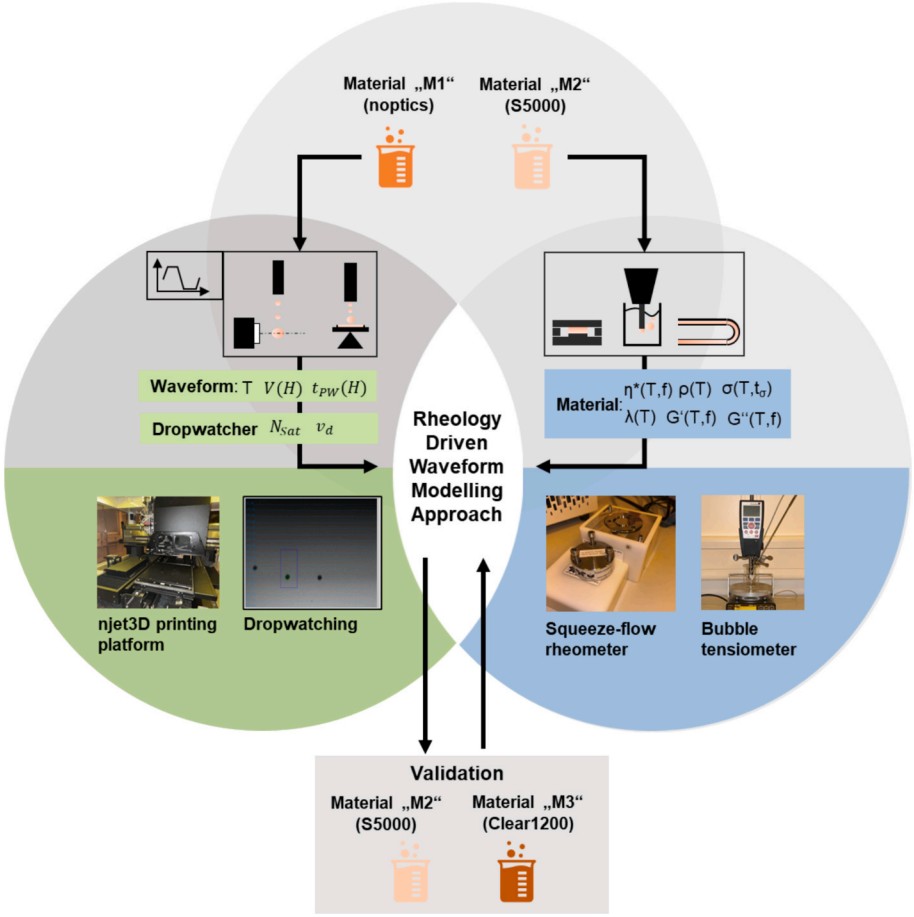

Fig. 3. Materials and methods for deriving a rheology-driven waveform modelling approach by correlating the input (material properties) and output (waveform and droplet behaviour) parameters relevant in inkjet printing

2.3. Modelling of the rheological data

Commercially available measurement devices cannot facilitate measurements at the typical dynamic range of inkjet printing. The following sections review the analytical models applied in this study to extrapolate measurements to frequency and temperature ranges relevant to inkjet printing.

2.3.1. Complex viscosity and viscoelasticity

Numerous mathematical models exist for estimating the viscosity at high shear rates, such as Power-law [66], Cross model [66] and Carreau-Yasuda [67]. Cross model is selected, because it captures the shear-thinning behaviour over a wide range of shear rate and the plateaus at low and high shear rates, which the Power-law fails to model. With Cross model, the initial complex viscosity η_0^* and the complex viscosity for very high shear rates η_∞^* can be modelled (Eq. (2)). C and n are material-dependent factors, and $\dot{\gamma}$ is the shear rate in the unit s^{-1}. Cross model is easier to fit compared to Carreau-Yasuda model, because it contains less parameters.

$$\eta^*(f) = \frac{\eta_0^* - \eta_\infty^*}{1 + (C\dot{\gamma})^n} + \eta_\infty^* \tag{2}$$

Storage (G') and loss modulus (G'') are fitted based on the Maxwell model with ω being the angular frequency, λ_{stor} and λ_{loss} the corresponding relaxation times, and E_{stor} and E_{loss} the elastic coefficients (Eqs. (3) and (4)). Maxwell model simulates a viscoelastic material by representing its viscous and elastic behaviour with a spring and damper element. The cross-over point of the storage and loss modulus defines the relaxation time of the material [48]. It is derived from the reciprocal of the cross-over angular frequency of storage and loss moduli [68].

$$G'(\omega) = E_{stor}(\omega\lambda_{stor})^2/(1 + (\omega\lambda_{stor})^2) \tag{3}$$

$$G''(\omega) = E_{loss}(\omega\lambda_{loss})/(1 + (\omega\lambda_{stor})^2) \tag{4}$$

In inkjet printing, the easiest way to adjust the rheological properties of the ink are by regulating the jetting temperature. The relationship between viscosity and temperature can be modelled by the Arrhenius equation [69] (Eq. (5)). The Arrhenius equation suggests that an activation energy threshold E_a (activation energy) is to overcome by applying thermal energy, so that the molecule motion accelerates. In the context of complex viscosity, a positive activation energy indicates that the viscosity drops with increasing temperature. This can be explained by an increased motion of molecules at higher temperature so that the fluidic molecules pass each other more easily. A is a pre-exponential factor and R is the gas constant [69]. The constant A can be interpreted as a viscosity value that is theoretically reached for a very high temperature. The constants A and E_a can be derived by plotting the complex viscosity logarithmically over the inverse value of the temperature in the unit Kelvin.

$$\eta^*(T) = A^* e^{\left(\frac{E_a}{RT}\right)} \tag{5}$$

2.3.2. Surface tension

The lowest surface age that can be applied with the bubble tensiometer is greater than the time period in which inkjet droplets are generated (less than 100 μs). Very few research exists, that models the surface tension over surface age. The empirical model proposed by Hua & Rosen (1988) is used to fit the dynamic surface tension [70] (Eq. (6)). σ_∞, σ_0, τ and s represent the surface tension at infinity surface age, zero surface age, the characteristic time, that is the time for the surfactant to reach the surface, and the fit parameter of this equation.

$$\sigma(t) = \sigma_\infty + \frac{\sigma_0 - \sigma_\infty}{1 + \left(\frac{t}{\tau}\right)^s} \tag{6}$$

Surface tension decreases with increasing temperature, as higher temperature accelerates movement of the liquid molecules so that the surfactant reaches the surface faster. Eötvös model provides a simple model with known molar volume V_M that states that the surface tension decreases in a linear manner for increasing temperature. The critical temperature T_c and constant k are determined from the coefficients of the linear fit approximating the surface tension over temperature in the unit Kelvin (Eq. (7)). The molar volume V_M is defined by the material's density ρ and molar mass m (Eq. (A.2), Appendix). M1, M2 and M3 are commercial materials, hence only little information regarding the chemical composition is available. As an estimate, the molar mass of the component that is known from the safety data sheet (this material normally makes up the majority of the ink), is taken. For M1, the molar mass of isobornyl acrylate is 208.3 $\frac{g}{mol}$ and for M2, a molar mass of 600 $\frac{g}{mol}$ is used, the value for polyethylene glycol. No equivalent models for heterogeneous materials are reported in the literature.

$$\sigma(t) = -\frac{k}{V_M^{\frac{2}{3}}}T + \frac{k}{V_M^{\frac{2}{3}}}T_c \tag{7}$$

2.4. Printing Platform and Jetting Waveform Settings

The material jetting printer njet3D (Notion Systems) is used in this study. Two printheads (KM1024iLHE-30, Konica Minolta) with a native droplet volume of 30 pl and native resolution of 360 dpi are mounted in this 3D printer. The printhead comprises of 1024 nozzles which are evenly distributed among four rows, resulting in each row's resolution to be 90 dpi. The printhead manufacturer reports that an inkjet ink with a viscosity of approximately 10 mPas and a surface tension of 31.7 mN/m can be printed on this printhead.

Each printhead behaves slightly different due to manufacturing tolerances. To ensure consistent performance, each printhead is calibrated with a model fluid in the factory. The driving voltage required to achieve the same jetting performance is then labelled on each printhead and saved in the EEPROM. The labelled voltage for the high voltage pulse specific for printhead 0 (PH0) is 12.2 V, and 11.9 V for printhead 1 (PH1). Material M1 is supplied to PH0 and Material M2 to PH1. PH0 is used for the validation with material M3.

A unipolar waveform is applied to the printhead for ejecting the droplets which consists of a high pulse section that corresponds to the expansion motion of the nozzle channel, followed by a low pulse section, during which the nozzle channel contracts (Fig. 4). This contraction will be neutralized in the next step and the necking of the droplet will be induced (cancellation) (Fig. 4). The amplitude and time duration of the different sections are interrelated. For instances, the driving voltage of the low pulse is half that of the high pulse section, and the pulse width of the low pulse and the cancellation section is twice as long as that of the high pulse section.

Accordingly, only pulse width $t_{Pw}(H)$ and the driving voltage of the high pulse $V(H)$ are varied in this study and the remaining parameters of the waveform are determined in relation to the two variables. The driving voltage is adjusted relative to the EEPROM value to ensure the results to be comparable between two different printheads. Table 1 gives an overview of the parameter range. The absolute values are listed in Table A1 in the Appendix.

2.5. Dropwatching

The correlation between multiple material properties and the jetting behaviour is to be established in this study. To ensure, that only the influence of the rheological parameters on the jetting behaviour is observed, and not the influence of other properties due to different ink compositions, dropwatching is conducted for the same ink at various temperatures (Table 1).

The built-in dropwatcher of the njet3D printer is used. During

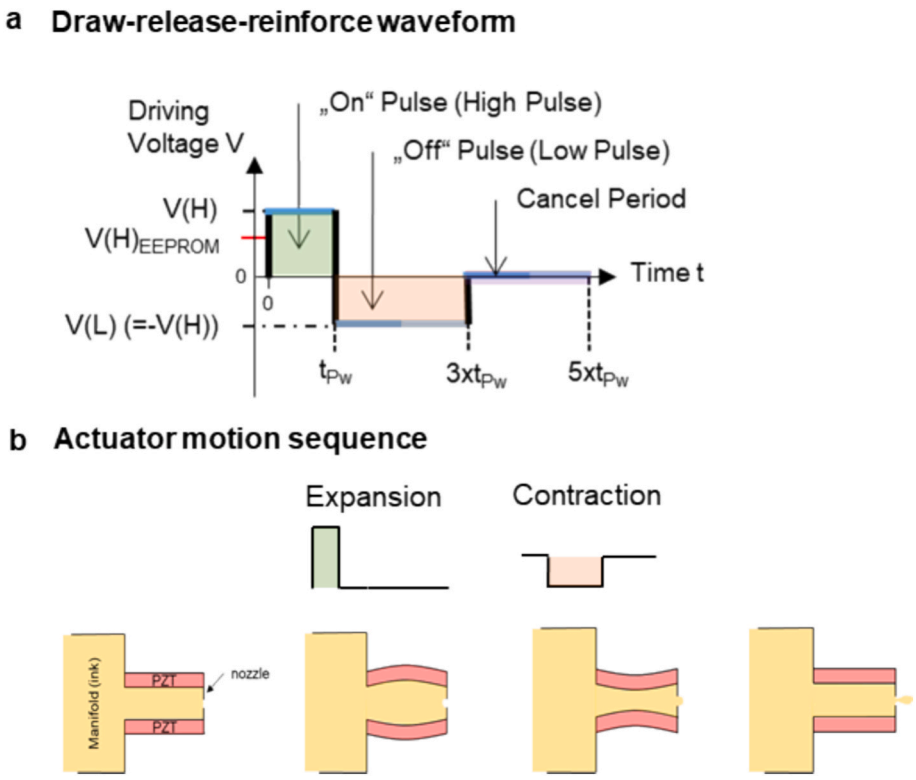

Fig. 4. Draw-release-reinforce waveform consisting of expansion, contraction and cancel period. (a) Waveform parameters is defined by voltages for high (V(H)) and low pulse (V(L)), and the pulse widths t_{PW}. (b) The piezo actuator deforms the nozzle channel according to the applied voltage.

dropwatching, the printhead is positioned between a strobe light and a camera. The strobe flash is synchronised with the jetting frequency, and an adjustable millisecond-scale delay between droplet ejection and the flash allows imaging at different distances from the nozzle.

22 nozzles are selected to be examined across the entire printhead range, namely the nozzle ranges 1–9, 120–136, 248–264, 504–520 and 1008–1023. Every fourth nozzle is activated during the dropwatching session as only one nozzle row on the printhead can be focused sharply. For example, while investigating the nozzle range 120–136, nozzles 120, 124, 128, 132 and 136 are jetting.

Droplet volume, number of satellite droplets, and position in ejection direction are determined based on the contour of the detected droplets during dropwatching. The results vary slightly depending on the brightness of the background. To maintain a similar background condition, the delay time is adjusted so that the droplets are captured within a distance to the nozzle plate of between 650 μm and 750 μm.

In addition, a weight-test is performed to determine the average jetted volume since the dropwatcher only examined a subset of nozzles. A print pattern with the size 72.0944 mm × 2.82 mm is jetted onto a petri dish of 80 mm diameter (40 layers, print resolution 360 dpi), meaning a total number of 1,635,200 droplets is ejected (one nozzle in the printhead is not working). By dividing the weight of the printed material by the number of printed droplets, the average droplet volume can be calculated.

2.6. *Jetting stability*

A 2D test pattern with 1024 vertical lines (aligned parallel to printing direction) is designed to evaluate the jetting stability, as each line corresponds to one nozzle (Fig. 5). The width of the test structure spans the entire printhead. Each line is staggered to prevent droplets printed from two neighboring nozzles to merge. The test pattern is printed with the native resolution of the printhead (360 dpi) and cured with UV-light immediately after print. The image of the printed validation test

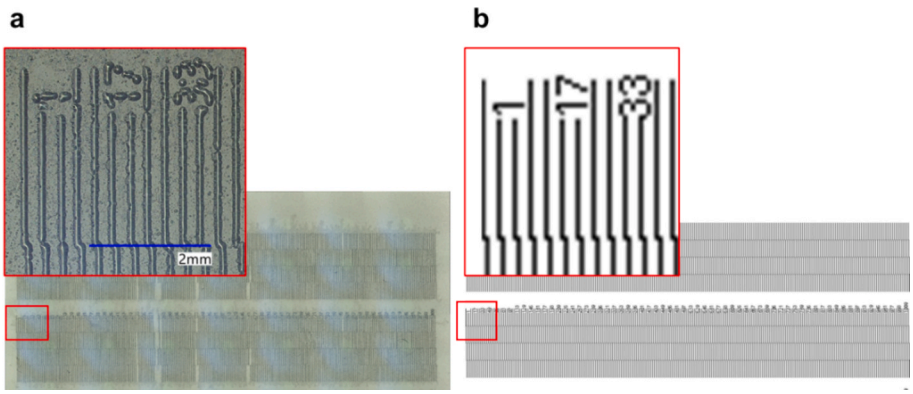

Fig. 5. Pattern for assessing the jetting stability. (a) Printed pattern. (b) Print image.

pattern is captured with the digital microscope Keyence VHX-7000. Both the jetting stability test and dropwatching are performed during the validation process.

3. Results and discussion

3.1. Material properties

3.1.1. Complex viscosity

Fig. 6(a and b) show the complex viscosity of M1 and M2 for the frequency range 1 Hz–10^4 Hz and at the temperatures 25–37.8 °C. The densities used for calculating the complex viscosities from the measured kinematic viscosity are listed in Table A2, Appendix. The complex viscosity is fitted with the Cross model (dashed line). All curves exhibit shear-thinning behaviour, meaning that the complex viscosity decreases with increasing frequency. Moreover, the complex viscosity reduces with increasing temperature. Material M2 is overall more viscous than M1.

Fig. 6c depicts the ratio of the complex viscosities at 10^4 Hz oscillatory frequency divided by the viscosity at 100 Hz of the modelled and measured values. The shear-thinning ratio is between 0.7 and 0.9. The shear-thinning behaviour of M2 is more pronounced than M1, as the ratios reported for M1 are located between 0.81 and 0.89, whereas M2 displays ratios from 0.7 to 0.81. The shear-thinning effect decreases with increasing temperature in a linear manner for both materials, evident in the positive slope and the good fitting of the data points with a linear function. In average, an increase of the temperature by 10 K leads to an increase in ratio by 0.09.

3.1.2. Viscoelasticity

Fig. 7 visualizes the loss and storage modulus, and the modelled curve based on the Maxwell equations. The storage modulus (G') is mostly present only in the lower and upper frequency range and exhibits a non-linear relationship with frequency. The loss modulus (G'') increases with increasing frequency. The extension of the data with the Maxwell model implies that the storage modulus overtakes the loss modulus between 10^4 and 10^5 Hz and plateaus at approximately 10^6 Hz, while loss modulus reduces considerably after the cross-over frequency (relaxation time). All in all, both storage and loss modulus decrease with increasing temperature.

3.1.3. Surface tension

The following Figures show the surface tension obtained for various surface ages and the corresponding modelled curve based on the Hua & Rosen equation (Fig. 8). Both materials show a rapid decrease of surface tension within few hundred milliseconds. The decreasing rate for M1 is larger (Fig. 8a), so that a static value is reached within 300 ms, whereas the surface tension of M2 is still slightly decreasing up to 2 s (Fig. 8b).

The ratios between the surface tension at 1000 ms and at 15 ms are ranging between 0.65 and 0.85 (Fig. 8c). Lower ratio means that the surface tension decreases with greater magnitude. M2 exhibits a lower rate, between 0.6 and 0.7, whereas M1 is showing a higher ratio, ranging from 0.8 to 0.85. While the ratios of M1 increases slightly with increasing temperatures, M2′s ratio is dropping minimally. For every 10 K difference, an absolute change of about 0.4 is observed.

3.1.4. Oscillation and damping behaviour

Fig. 9 shows the result of the piezo oscillation measurements for both M1 and M2. The black curve depicts the input voltage (2 V) for triggering the oscillation of the ink. The difference between the peak and the trough level of the oscillation curve increases with elevated temperature (Fig. 9a and b, blue, primary y-axis). The lower the temperature, the less

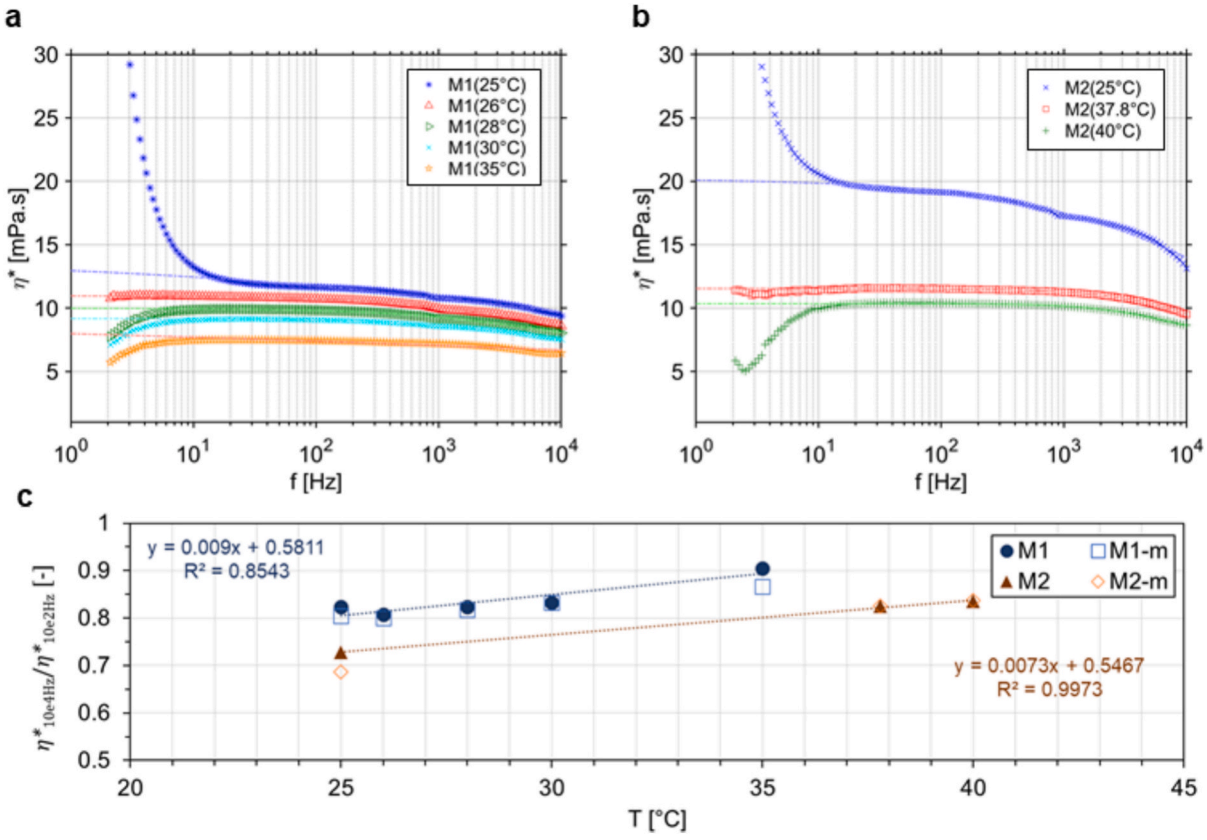

Fig. 6. Complex viscosity (dashed lines, Cross model, coefficients in Table A3). (a) Material M1 is measured at 25 °C, 26 °C, 28 °C, 30 °C and 35 °C. (b) Material M2 is examined at 25 °C and 37.78 °C. (c) Ratios of complex viscosity at frequencies 10^4 Hz and 10^2 Hz of materials M1 and M2 (–m, measured values; no suffix, modelled value).

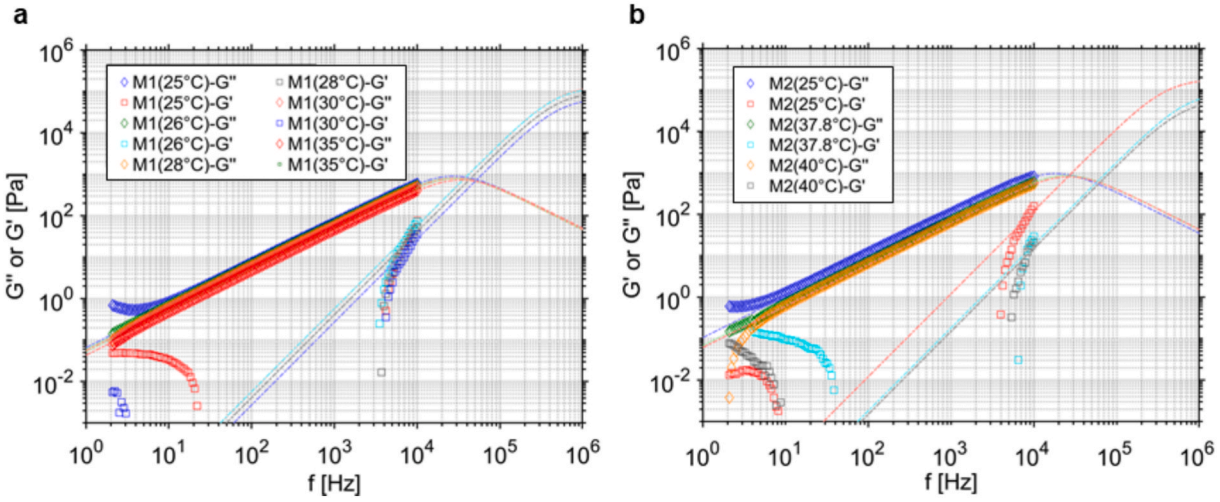

Fig. 7. Storage (G') and loss modulus (G''), and modelled curve (dashed lines, Maxwell model, coefficients in Table A3). (a) Material M1 measured at 25 °C, 26 °C, 28 °C, 30 °C and 35 °C. (b) Material M2 measured at 25 °C, 37.8 °C and 40 °C.

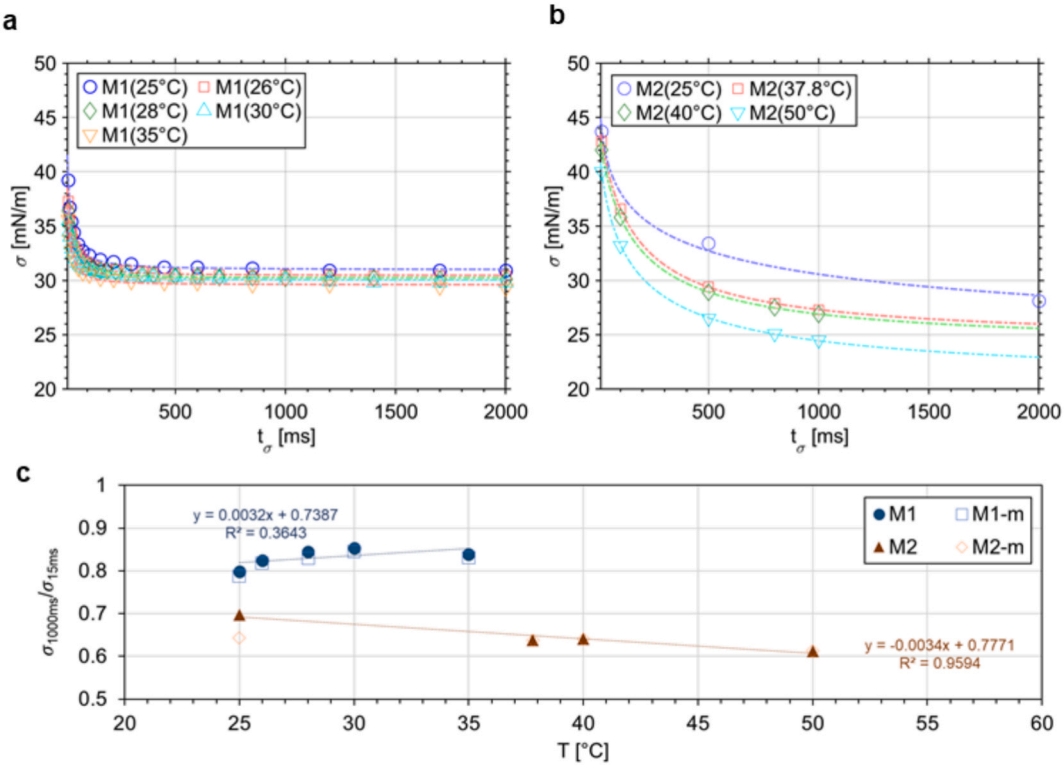

Fig. 8. Dynamic surface tension (dashed lines, Hua & Rosen model, coefficients in Table A3). (a) Material M1 measured at 25 °C, 26 °C, 28 °C, 30 °C and 35 °C. (b) Material M2 measured at 25 °C, 37.8 °C, 40 °C and 50 °C. (c) Ratio between surface tension at surface ages 1000 ms and 15 ms (−m, measured value; no suffix, modelled value).

residual oscillation is present after the initial peak. The curve reported for M2 at 25 °C is at roughly 0.34 V and particularly flat, almost following the shape of the input voltage curve.

The time required for the oscillated material to reach the peak value shortens with increasing temperature (Fig. 9b, orange, secondary y-axis), although the change is relatively small for M1, whereas for M2 is it considerably large due to the long peak time $t_{osc,p}$ reported for 26 °C (around 220 μs). M2 at 38 °C, on the contrary, is reporting similar oscillation behaviour as M1 (around 90 μs) (Fig. 9b).

3.1.5. *Temperature curves*

In the following Figure, the modelled temperature curve for the properties complex viscosity, storage modulus, relaxation time, dynamic surface tension and density at various temperatures are displayed (Fig. 10). These properties are selected because of the relevance for the satellite droplet formation, as explained in the previous literature review Section. Table 2 shows the coefficients of the Arrhenius and Eötvös model determined for M1 and M2. The coefficients of the linear fit for density, storage modulus and relaxation time are displayed in Fig. 10f.

In plot Fig. 10a, the complex viscosity modelled by Cross and Arrhenius model for the frequency 10^5 Hz is displayed in the

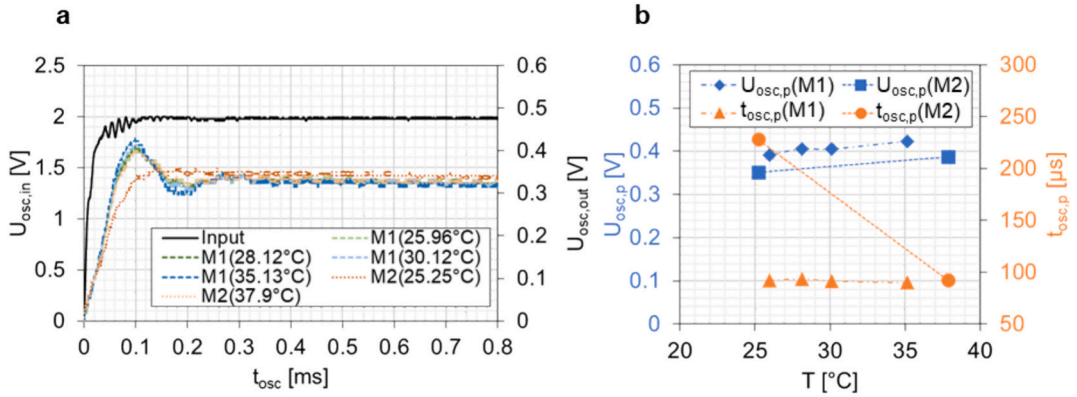

Fig. 9. (a) Oscillation and damping behaviour of M1 and M2 at 26 °C to 38 °C. Primary y-axis show the input voltage, secondary axis indicates the signal output of the piezo element after excitation by the input voltage. (b) Peaks of output signals. Data can be found in Table A7.

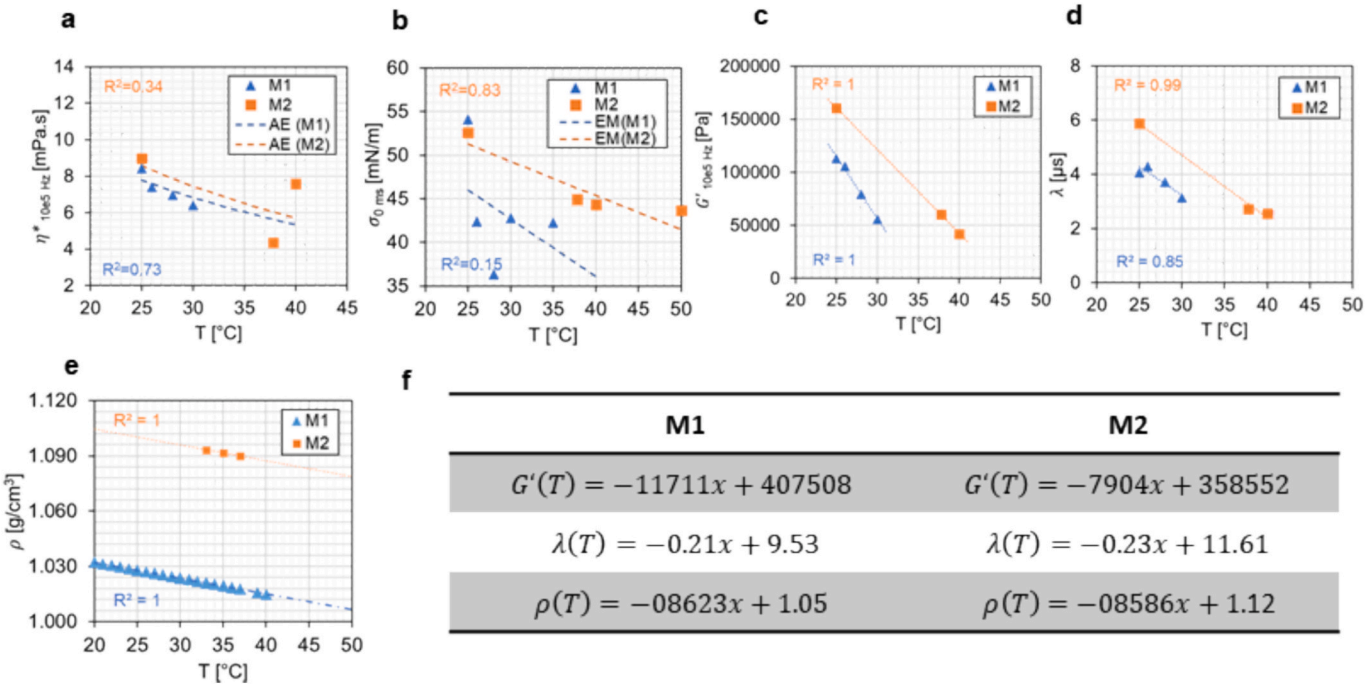

Fig. 10. Temperature dependency of rheological properties of material M1 and M2. (a) Complex viscosity (dashed lines, Arrhenius model (AE)). (b) Dynamic surface tension (dashed lines, Eötvös model (EM)). (c) Storage modulus (linear fit). (d) Relaxation number (linear fit). (e) Density (linear fit). (f) Coefficients of the linear fitted properties.

Table 2
Constants and coefficients of the Arrhenius and Eötvös model for M1 and M2 for describing the temperature dependency.

Arrhenius model		M1	M2
A	$[Pas]$	$3.054E-06$	$1.776E-06$
E_a	$[\frac{J}{mol}]$	19442.289	21026.106
Eötvös model			
T_C	$[K]$	369.834	436.272
k	$[\frac{Jmol^{\frac{2}{3}}}{K}]$	$2.21388E-06$	$2.47812E-06$

temperature range 25 °C to 40 °C. The complex viscosity decreases with increasing temperature. The slightly greater activation energy E_a for M2 (Table 2) is aligning with the observation, that the complex viscosity of M2 is more sensitive to a change of temperature, hence subject to more rapid loss of viscosity. For an infinite temperature, M2 reaches a lower viscosity (lower A value). The goodness of the fit of M2 is less than M1, because of the large difference of the measured complex viscosity at higher temperatures.

In Fig. 10b, the modelled surface tension at zero surface age is displayed. The parameters of the Eötvös model for M1 and M2, critical temperatures T_C and constants k_M, are listed in Table 2. The negative slope of the modelled curve indicates that with enhanced temperature, the surface tension diminishes. In particular, the curve of M1 is steeper, and the intersect value lower than M1, implying that the overall surface tension of M2 is expected to be greater than M1.

Storage modulus (Fig. 10c) and relaxation number (Fig. 10d) reduce with increasing temperatures. M2 is overall exhibiting a higher storage modulus than M1, which leads to a higher relaxation number for M2 as well. The density of both materials decreases with increasing temperature in a linear manner (Fig. 10e). The rate of decrease for both material is very similar (around $-0.86\,\frac{kg}{m^3}$). Overall, M1 is less dense than M2.

Elevating the temperature facilitates a reduction of all rheological properties.

3.2. Jetting behaviour

3.2.1. Droplet volume verification and jetting stability

Fig. 11a compares the droplet volumes obtained via the dropwatcher $V_{d,dw}$ to the value obtained by the weight-test $V_{d,w}$. The printed pattern for verifying the jetting stability of each nozzle is displayed on the right-hand side of the figure (Fig. 11b and c). The droplet volume ratio of M1 is considerably stable and stays around 140 %. On the contrary, M2 displays a considerably difference between the obtained droplet volumes. For material M2 at 25 °C, the dropwatcher-based droplet volume is four times greater than the weight-test based result, whereas for 37.8 °C the ratio drops to 150 %. The corresponding print pattern at 25 °C shows an irregular print with multiple gaps due to non-firing nozzles, hinting at an instable jetting behaviour, while just by increasing the temperature to 37.8 °C, almost all nozzles are firing.

3.2.2. Pulse width and driving voltage

The droplet behaviour at a fixed driving voltage and under varying pulse widths reveals a quadratic relationship between pulse width and droplet velocity (Fig. A1). This means, that any pulse widths greater or lower than the optimum value decreases the droplet velocity. The printhead geometry and the acoustic behaviour of the material, such as speed of sound, dictates the optimal pulse width. The speed of sound is proportional to the square root of density, hence dependent on the temperature. A higher temperature reduces the density, which results in a shorter optimum pulse width. For M2, a maximum velocity of the droplet is reached around 7.61 ± 0.2 µs at 25 °C, and 7.28 ± 0.13 µs at 37.8 °C, the optimum pulse width at the corresponding temperature. All in all, the higher the temperature, the smaller the standard deviation and the shorter the optimum pulse width becomes. For M1, a similar trend is visible. At 26 °C, the optimum pulse width is observed to be around 7.38 ± 0.25 µs, whereas the pulse width for 35 °C is 7.22 ± 0.1 µs. In general, adjusting the pulse width by ±1 µs around the optimum pulse width reduces the droplet velocity by roughly 0.5 to 1 m/s.

The variation in droplet velocity with different driving exhibits a linear relationship (Fig. A2). Fig. 12 visualizes the droplet velocity of all dropwatching results over the relative driving voltage and displays images of dropwatching trials. The colour scheme of the data points corresponds to the number of satellite droplets. The corresponding jetting temperatures are annotated in the plots. It is evident, that for both materials, green data points – single droplet jetting – cluster around a droplet velocity range between 1.5 and 3 m/s. With increasing droplet velocity, the number of satellite droplets increases. The linear relationship between driving voltage and droplet velocity varies slightly between material M1 and M2, evident in the different slope and y-intersect values (Table A6).

3.3. Discussion

3.3.1. Jetting stability

The droplet volume obtained by Weight-test suggests that the weighted droplet volume of M2 at 25 °C is only ¼ of the droplet volume displayed during dropwatching. A test pattern covering the entire range of nozzles confirms that some nozzle rows are subject to irregular jetting which explains the missing droplet volume when assessing over the entire range. Several factors can cause nozzles to jet irregularly. The piezo oscillation measurements reveal that no residual oscillations are present for M2 at 25 °C, the unstable jetting is most likely caused by insufficient kinetic energy so that the droplet cannot detach from the nozzle exit [32]. Therefore, it is advised to examine the general jettability after dropwatching before finalizing the waveform selection.

Nevertheless, at stable jetting condition, the weighted droplet volume is overall greater than the volume observed on the dropwatcher (by roughly 140 %). This difference equals to a droplet volume difference of 10 pl, which is equivalent to a deviation in droplet diameter of about 5 µm. Since the droplet volume is determined based on the captured image, the observed deviation could result from an inaccurate contour detection or insufficient resolution of the camera.

3.3.2. Rheological properties

The significant differences in rheological behaviour between M1 and M2 can largely be attributed to the distinct polymer types used in each ink formulation. M2 contains PEG molecules which create a solution with strong intermolecular hydrogen, therefore M2 exhibits overall higher viscosity than M1. Further, the viscosity of M2 decreases more significantly with increasing temperature than M1. This may be attributed to the higher flexibility and less entangled chains in PEG compared to acrylate monomers.

Strong intramolecular bonds also hinder the rapid reduction of surface tension, resulting in M2 displaying a higher surface tension at lower surface age. Furthermore, this leads to an increased storage modulus as well, as the enhanced molecular attraction provides greater resistance to deformation. The material is able to store more energy before deforming. A higher surface tension typically requires a higher concentration of surfactant to lower the value, which is accompanied by more pronounced foaming, as observed during the surface tension measurement of M2.

Generally, a discrepancy between the modelled and measured surface tension value is present. For instances, while the surface tension of isobornyl acrylate (M1) is 33 mN/m, the model predicts a higher surface tension for 0 ms surface age (43.56 ± 6.5 mN/m). This may be

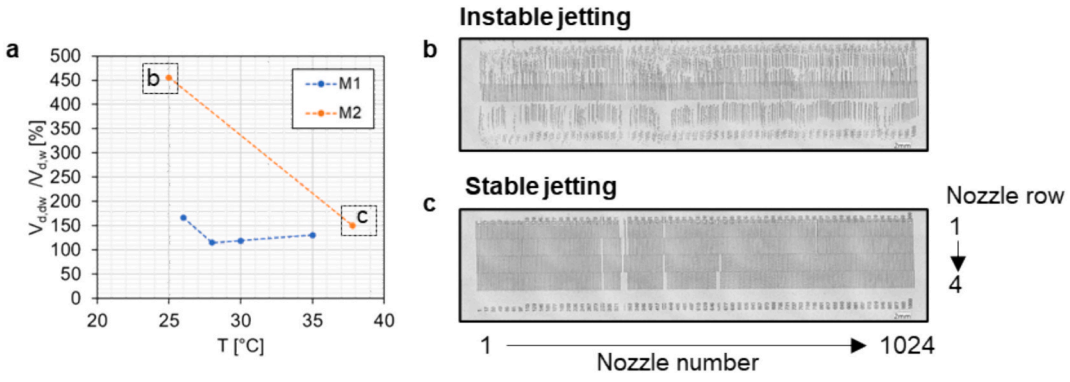

Fig. 11. (a) Ratio of the average droplet volume determined by weight-test $V_{d,w}$ and droplet volume obtained by dropwatching $V_{d,dw}$ of both materials M1 and M2. Average droplet volumes are listed in Table A4. (b) Instable jetting behaviour of material M2 at 25°C, evident in non-firing nozzles and excessive misting. (c) Stable jetting of material M2 at 37.8°C.

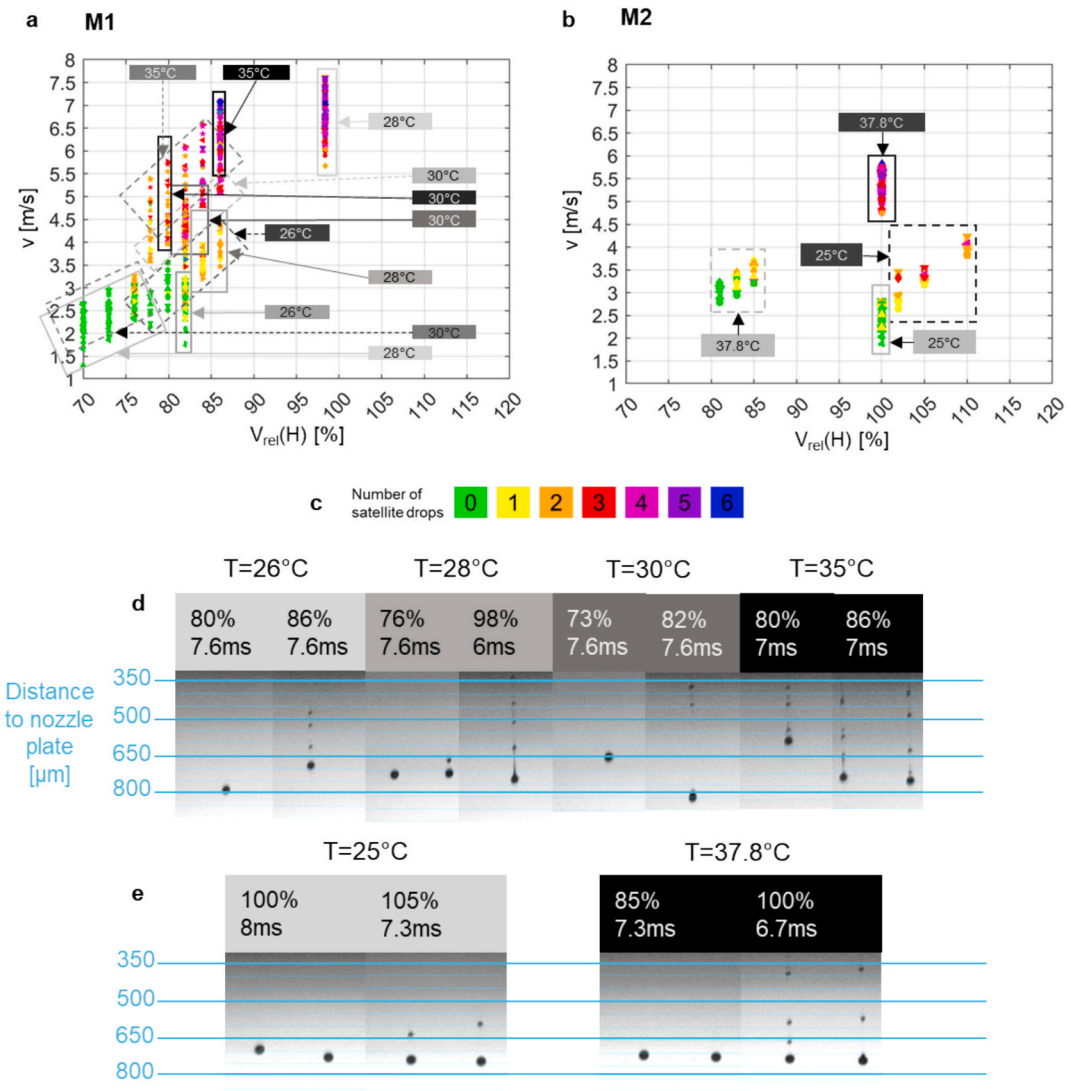

Fig. 12. Effect of driving voltage and jetting temperature on droplet formation. Droplets jetted at the same temperature are grouped within boxes. (a) Droplet velocity profile of material M1 jetted at 26°C, 28°C, 30°C, 35°C (b) Droplet velocity profile of material M2 jetted at 25°C and 37.8°C. (c) Satellite droplet count represented by distinct colours. (d, e) Corresponding images of M1 and M2 captured on dropwatcher. V_{rel}(H) is the driving voltage relative to the EEPROM reference value of the printhead (PH0 (M1): 100% = 12.2 V, PH1 (M2): 100% = 11.9 V)

attributed to the presence of other unknown components in the ink that significantly increases the surface tension. Additionally, the Hua & Rosen model is an empirical model, and might show inaccuracies in very low surface ages. In theory, the surface tension at 0 ms surface age should be same for all temperatures, since no surfactant are mobilised at this point.

The measured density of M1 is 1027 $\frac{kg}{m^3}$, which is notably higher than the density reported for isobornyl acrylate at 25 °C (986 $\frac{kg}{m^3}$). This difference suggests that other components in the ink dominate the ink's density. The material data sheet of material M2 states a density of approximately 1100 $\frac{kg}{m^3}$ $at 20^{\circ}C$, which is close to the value predicted based on the regression coefficients (1104 $\frac{kg}{m^3}$). Overall, all properties decrease with higher temperature, however the magnitude of the reduction varies, as each ink's formulation is different.

3.3.3. Pulse width

The peak time determined by the piezo oscillation measurement allows a rough estimate of the channel length of the printhead. By considering the optimum pulse width $t_{PW,opt}$, obtained via dropwatching, and peak time $t_{osc,p}$ derived from the piezo oscillation measurement, the channel length of the printhead l_{PH} can be estimated according to the following Eq. (8). The channel length l_{rheo} of the squeeze-flow rheometer is 20 mm.

$$\frac{l_{rheo}}{t_{osc,p}} = \frac{l_{PH}}{t_{PW,opt}} \tag{8}$$

To estimate the pulse width, the results of M1 (Table A5 and Fig. 9a) are utilized for the calculation. The approximate channel length is calculated for each temperature and averaged. The resulting average channel length of the printhead is 1585 µm ± 29 µm. Fig. 13 visualizes both the estimated and actual optimum pulse width determined for M2. It is worth mentioning that the left most data point of M2 curve is beyond the value range even though the standard deviation has been taken into consideration. Besides, all estimated values are close to the measured optimum pulse widths. This implies, that the estimated printhead channel length is close to the real value.

In this study, both materials M1 and M2 exhibit relaxation times (<5.88 µm) that are shorter than the optimum pulse width which is governed by the acoustic properties of the material and the geometry of the printhead. To ensure stable jetting behaviour, the pulse width should exceed the relaxation time, allowing the material to behave

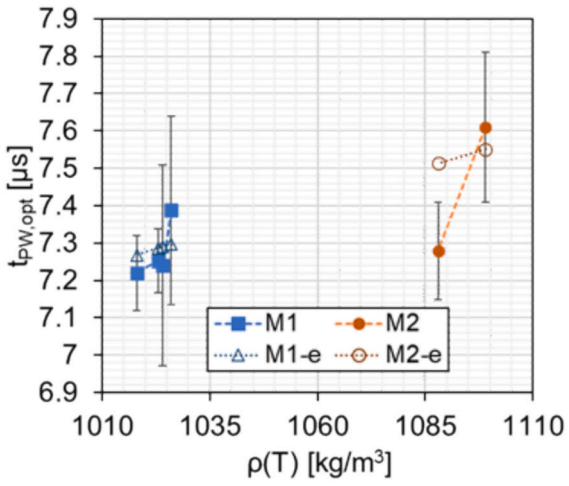

Fig. 13. Measured and estimated (suffix −e) optimum pulse width $t_{PW,opt}$ over density of the ink $\rho(T)$.

predominantly as a viscous fluid and thereby minimizing the influence of elastic properties that can lead to instability in inkjet printing. The identified optimum pulse widths of M1 and M2 fulfill this requirement and do not need further adjustment.

3.3.4. Driving voltage

Fig. 12 indicates that the higher the driving voltage, the faster the ejected droplet becomes, and the more satellite droplets are produced. The observed relationship between droplet velocity and satellite droplet can be explained as follows: At higher droplet velocity, the ligament is thinned out more rapidly. As the radius of the ligament decreases, it becomes more susceptible to disintegration into satellite droplets due to surface tension. Consequently, the formation of satellite droplets is not only governed by the rheological properties of the ink, but also by the driving voltage, since it directly influences the droplet velocity. Table 3 summarizes the velocity range associated with a particular number of satellite droplets. For droplet travelling with a velocity less than 3 m/s, no satellites are observed. Similarly, Zhang et al. (2015) observed a similar positive correlation between velocity and the number of satellite droplets, with the minimum droplet speed observed being approximately 3 m/s [71]. The droplet velocities recorded for droplets without any satellite droplets remain above the minimum jetting velocity of 1.6 m/s.

Fig. 14 depicts the rheological properties at the corresponding jetting temperatures over the speed of the droplets that are jetted with a relative driving voltage of 78 % and 86 %. The data label indicates the jetting temperature in the unit °C. The upper x-axis indicates the number of satellite droplets that is to be expected when exceeding the corresponding velocities (lower x-axis).

When increasing the temperature, all rheological properties reduce in value. With lower viscosity, the viscous force of the material decreases, resulting in less kinetic energy being dissipated, which leads to a faster-moving droplet. An ink with lower surface tension requires less kinetic energy to overcome the surface tension of the meniscus at the nozzle, allowing more energy to be directed toward droplet ejection. A reduction in storage modulus means that less amount of the kinetic energy during droplet ejection is stored as an elastic energy, resulting in more energy transferred into propelling the droplet from the printhead.

In Fig. 14a, an increase in the number of satellite droplets from 0 to 3 by elevating the driving voltage from 78 % to 86 % is observed even though the complex viscosity of material M1 did not change. This behaviour is apparent also for surface tension (Fig. 14b), relaxation number (Fig. 14c) and storage modulus (Fig. 14d). This implies that the rheological parameters are not the sole determining factors for predicting the onset of satellite drops, contrary to what several previous publications have assumed [39]. Fig. 14f shows that droplet velocity increases with elevated temperature in a linear manner.

Table 3
Droplet velocity defines the number of satellite droplets.

Velocity range [m/s]	Number of satellite droplets [–]
1.6	Jetting threshold (Equation (A.3), Appendix) [32]
<3	0
3–3.8	1
3.5–4	2
4–5	3
5–6	4
5.5–7	5
>7	6

4. Rheology-driven modelling and experimental validation

4.1. Rheology-driven regression modelling

From the former Section, several conclusions can be drawn:

- The number of satellite droplets can be linked to distinct droplet velocity zones (Section 3.3.4)
- Variation in pulse width yields only marginal change in droplet velocity. The optimal pulse width is reached, if any variation, whether an increase or a decrease, reduces the droplet velocity. Once the optimum pulse width is determined, the optimization of waveform should primarily focus on adjusting the driving voltage (Section 3.2.2).
- Driving voltage and droplet velocity are correlated in a linear manner (Section 3.2.2).
- The coefficients of the linear relationship are influenced by the rheological properties of the ink (Section 3.2.2).
- Changing the jetting temperature, which in turn alters the density, surface tension, complex viscosity and storage modulus, influences the resulting droplet velocity (Section 3.3.4).

Based on these findings, it is inferred that a linear combination of all relevant rheological properties should be deployed to predict the coefficients of the linear equation describing the relationship between driving voltage and droplet velocity. Each rheological parameter is assigned a scalar coefficients, namely $\alpha_{1,m}$ and $\alpha_{1,q}$ for complex viscosity, $\alpha_{2,m}$ and $\alpha_{2,q}$ for surface tension, $\alpha_{3,m}$ and $\alpha_{3,q}$ for density and $\alpha_{4,m}$ and $\alpha_{4,q}$ for storage modulus (Eqs. (9) and (10)). Relaxation time is not considered, because it is dependent on the storage modulus. The scalar coefficient reflects the contribution of a specific rheological property to the slope and y-intersect.

$$\alpha_{1,m}\,\eta_{10e5Hz}^{*} + \alpha_{2,m}\sigma_{t=0ms} + \alpha_{3,m}\rho(T) + \alpha_{4,m}G'_{10e5Hz} = m \tag{9}$$

$$\alpha_{1,q}\,\eta_{10e5Hz}^{*} + \alpha_{2,q}\sigma_{t=0ms} + \alpha_{3,q}\rho(T) + \alpha_{4,q}G'_{10e5Hz} = q \tag{10}$$

These scalar coefficients are solved by constructing a system of four linear equations, using the measured rheological properties of M1 and M2 and the corresponding droplet velocities obtained under four different experimental conditions. The rheological values are listed in Table A2. The least square method is utilised to solve this system of equations. The solution of this linear system of equations is

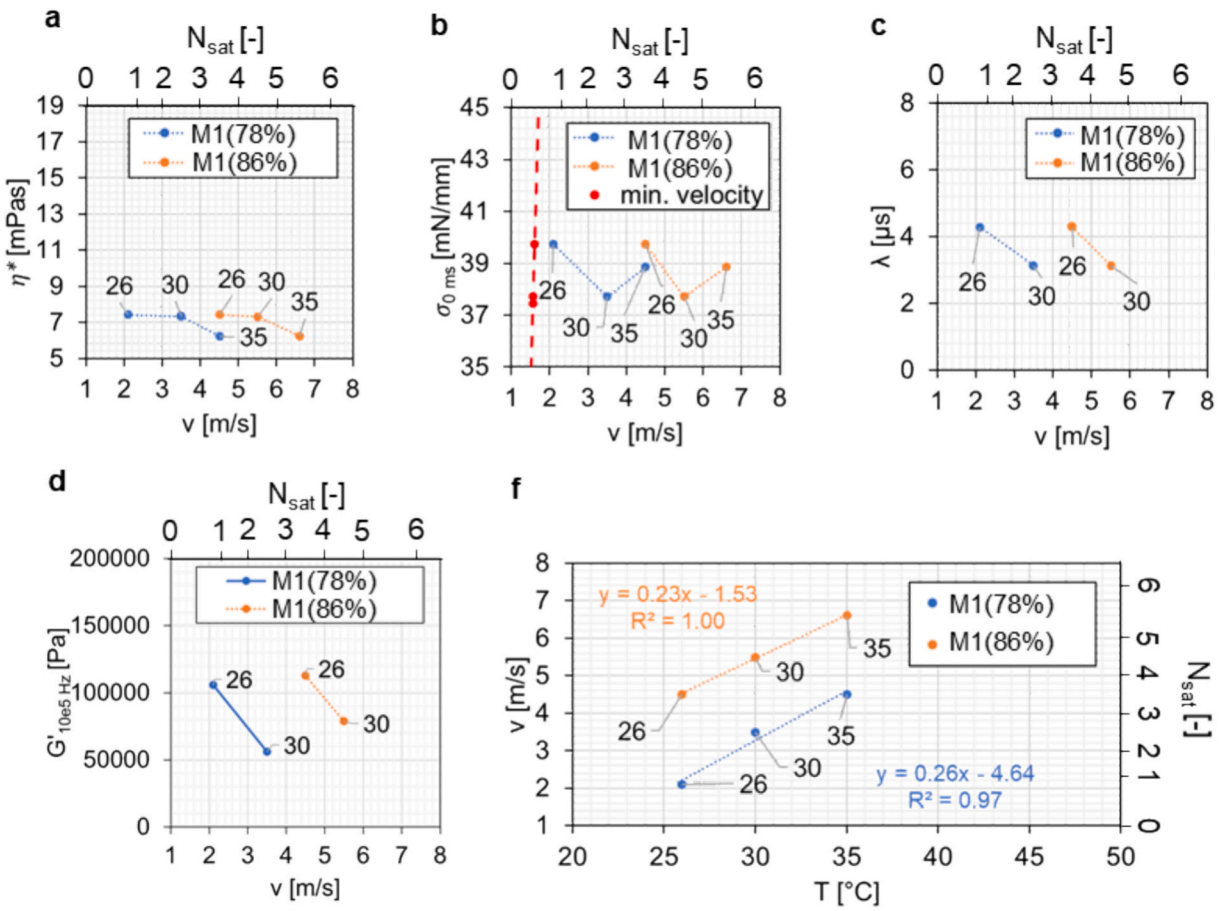

Fig. 14. The correlation between droplet velocity, jetting temperatures, number of satellite drops and rheological properties of material M1 jetted at 78 % and 86 % driving voltage. (a) Complex viscosity at frequency 10^6 Hz. (b) Surface tension at 0 ms surface age. (c) Relaxation number. (d) Storage modulus G' at frequency 10^6 Hz. (e) Oscillation peak amplitude. (f) Correlation between temperatures and droplet velocity.

$$\alpha_{1,m} = 0.02391 \frac{\frac{m}{s}}{\frac{V[\%]}{mPas}},$$

$$\alpha_{2,m} = 0.00082 \frac{\frac{m}{s}}{\frac{V[\%]}{\frac{mN}{m}}},$$

for the slope and

$$\alpha_{3,m} = 0.03688 \frac{\frac{m}{s}}{\frac{V[\%]}{\frac{g}{cm^3}}},$$

$$\alpha_{4,m} = -8.3*10^{-7} \frac{\frac{m}{s}}{\frac{V[\%]}{Pa}}$$

$$\alpha_{1,q} = -1.44138 \frac{\frac{m}{s}}{mPas},$$

$$\alpha_{2,q} = -0.0748 \frac{\frac{m}{s}}{\frac{mN}{m}},$$

for the y-intersect.

$$\alpha_{3,q} = 0.49954 \frac{\frac{m}{s}}{\frac{g}{cm^3}},$$

$$\alpha_{4,q} = 3.048*10^{-5} \frac{\frac{m}{s}}{Pa}$$

The residuals are 0.00094 and 2.1864, respectively.

The scalar coefficients for the slope equation imply that a higher viscosity, surface tension and density, and a lower storage modulus increase the sensitivity, as the slope describes the sensitivity of the droplet velocity to changes in driving voltage. With regards to the y-intersect equation, it can be concluded that a higher viscosity and surface tension, and a lower density and storage modulus value reduce the y-intersect. Y-intersect is positively correlated to the droplet speed of the ejected droplet and inversely linked to the minimum driving voltage required to eject a droplet. Thus, a lower y-intersect means that the material will overall jet with lower droplet velocity for the same driving voltage setting and that the driving voltage threshold becomes higher. With this solution, following methodology can be applied to estimate the parameters for a bipolar waveform at any jetting temperature (Fig. 15).

First, the density is to be determined, followed by the measurement of loss and storage modulus and complex viscosity. The results are extended by Cross model (complex viscosity) and Maxwell model (viscoelasticity) to a higher frequency range, such as 10^5 Hz. Dynamic surface tension should be measured at a minimum of three different surface ages due to the non-linear relationship. The fitting with Hua & Rosen model identifies the surface tension at 0 ms surface age which is closer to the typical surface age of a droplet in-flight which is between 100 and 300 µs [12]. The complex viscosity for different temperatures can be modelled by the Arrhenius rule, whereas the Eötvos rule is applied for surface tension. Storage modulus and density are correlated to temperature in a linear manner. These properties derived from the modelling are then applied to the printhead-specific regression model for generating a droplet velocity-driving voltage curve. The final step is

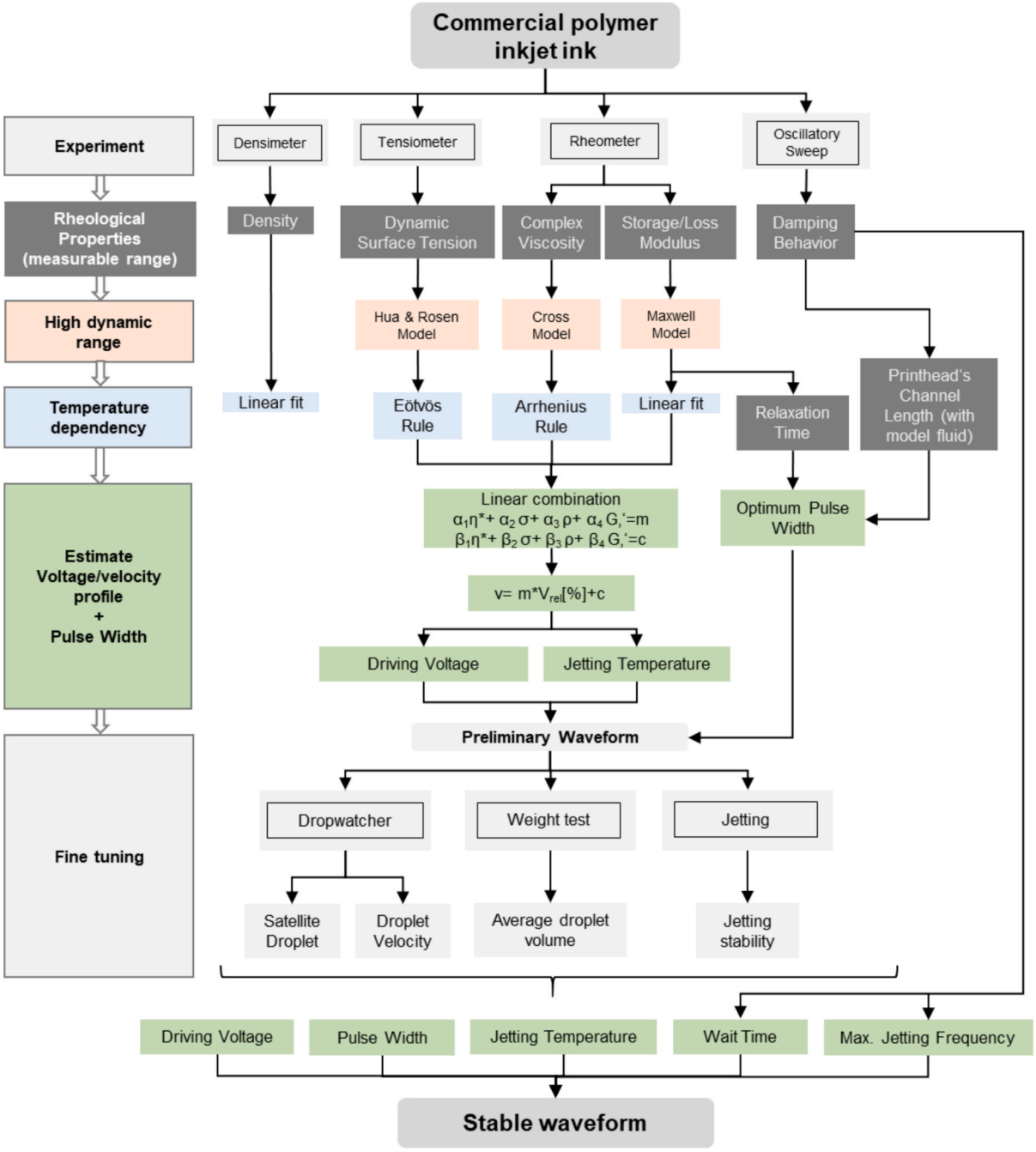

Fig. 15. Rheology-driven approach for determining the jetting temperature and waveform parameters (unipolar waveform) for a stable jetting performance.

to either find a driving voltage or a jetting temperature that yield a droplet velocity of around 3 m/s, which enables satellite-free single droplet jetting. Printhead-specific thresholds for surface tension and viscosity or voltage and pulse widths are to be considered in this search.

Meanwhile, the pulse width of the waveform is estimated from the piezo oscillation measurement, provided that the nozzle channel length is known (Section 3.3.3). If the relaxation time of the material is longer than the estimated pulse width, the pulse width must be extended to at least the relaxation time or longer to prevent instable jetting behaviour [38]. It is suggested to print the jetting stability print to verify the stability of the waveform.

4.2. Experimental validation

The proposed methodology is validated with two materials: first, M3, which served as the primary validation ink, and second, M2, tested at temperatures that were not used during the model-derivation phase. For M2, the validation is conducted at the jetting temperatures 25 °C, 30 °C, 35 °C and 40 °C, whereas for M3, the droplet formation at 26 °C and 45 °C is examined.

The rheological properties and modelled parameters of M3 can be found in the Appendix. The Cross model of M3 predicts a very low complex viscosity at 10^5 Hz (around 4 mPas at 25 °C and 0.9 mPas at 50 °C) which are considered unreasonable, because the printhead would not be able to jet the material, contrary to the results observed during the validation trials. Therefore, in order to obtain a more reasonable value, the shear-thinning ratios observed in Section 3.1.1 are averaged (slope 0.00815 $\frac{mPas}{Hz}$, y-intersect 0.5639 *mPas*) and applied to the measured value to estimate the viscosity at 10^5 Hz. This results in a

complex viscosity of 12 mPas at 25 °C and 7 mPas at 50 °C.

M3 could be successfully jetted at 26 °C. According to the modelled curve, the surface tension at this temperature is approximately 50 mN/m, while the viscosity is around 11 mPas. This means, that the printhead is capable of ejecting droplets with viscosity and surface tension greater than 40 mN/m and 8 mPas, despite M1 and M2 failed to be jetted. This observation could imply that the jettability threshold of the printhead seems not to be only governed by these two properties, which is also reported by previous studies [38]. Another reason for the discrepancy is the inaccuracy of the model.

The pulse width value determined for M3 is deviating slightly from the real value. The piezo oscillation measurement results in a peak time of 78 μs at 26 °C and 71 μs at 50 °C for M3. With a printhead channel length of 1585 μm, an optimal pulse width of 6.1 μs (25 °C) and 5.6 μs (50 °C) are estimated. Since the relaxation times at both temperatures (6.5 μs at 25 °C and 6.9 μs at 50 °C) exceed the pulse width, the optimal

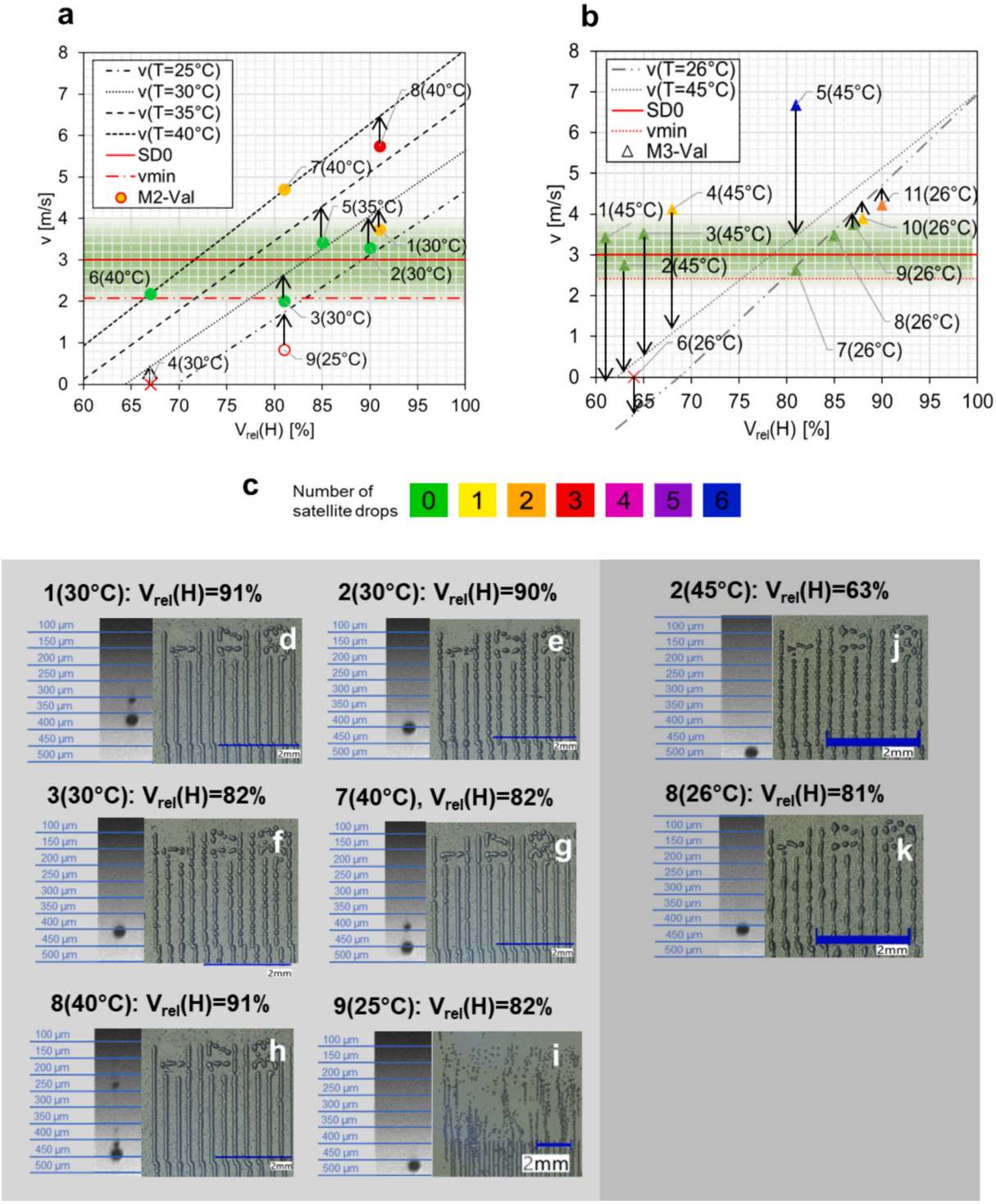

Fig. 16. Modelled droplet velocity and actual droplet velocity of M2 and M3 at varying driving voltage. (a) Validation results of M2 at 25 °C, 30 °C, 35 °C and 40 °C. (b) Validation results of M3 at 26 °C and 45 °C. (c) Satellite droplet count represented by distinct colours. (d–k) Corresponding results of dropwatcher and printed test pattern.

pulse width must be at least equal to the relaxation time. Dropwatching at 26 °C discloses that the optimum pulse width is around 7.5 μs, thus 15 % greater than the relaxation time. Relaxation time is determined by the intersection point of the modelled loss and storage modulus. For all three materials, it is generally observed that the loss modulus appears only in very high frequency range. Due to the restriction of the rheometer of measuring only up to 10^4 Hz, only few data points of loss modulus are captured. The number of data points might be insufficient to provide a fitted model that is accurate beyond the measured frequency range, thus affecting also the accuracy of relaxation time. The pulse width of 7.5 μs is used for the validation at 50 °C as well.

Fig. 16 displays the modelled curves quantifying the relationship between driving voltage and droplet velocity at specific jetting temperatures, and the validated data points for M2 and M3 (Fig. 16a and b). The modelled coefficients are listed in the Appendix. The data points represent the actual droplet velocity according to the dropwatcher. Below these two plots, the corresponding dropwatching results and microscopic images of the printed jetting stability pattern are shown. The data points utilize the same colour coding as in previous Figures for indicating the number of satellite droplets, namely zero (green), one (yellow) and two (orange) satellite droplets (Fig. 16c). The red horizontal line marks the average droplet velocities of the single droplet zone (3 m/s). The dashed line below marks the minimum velocity based on the equations of Duineveld et al. [72]. The arrow points at the corresponding temperature-specific model curve to which the data points are associated. The experimentally obtained data are validated against the model.

Generally, the observed number of satellite droplets of the experimental data points in Fig. 16 are within the velocity zones defined in previous Section. The microscope images present the difference of a structure printed with and without satellite droplets. For instances, Fig. 16e,f,j,k are all structures printed without satellite droplets. The printed lines still exhibit distinct droplet shapes. In Fig. 16d and h, the additional satellite droplet bridges the main droplets, resulting in straight lines without necking.

Fig. 16a displays the validated data for M2. The prediction of the droplet velocity for jetting temperature 40 °C is precise up to a driving voltage of 90 %. For lower temperatures, an overall deviation of about less than + 1 m/s (<25 %) are observed, although the model curves consistently overperform, meaning that a higher droplet velocity is estimated by the regression model. Data points 4 and 9 in Fig. 16a are predicted to be not jettable, which are confirmed by the dropwatching experiment. Fig. 16i illustrates such a case where, if the minimal velocity is not reached, inconsistent jetting occurs, accompanied by irregular nozzle failure. The small dots originate from misting, probably caused by an excessive accumulation of material around the nozzle plate, because the kinetic energy provided by the driving voltage is insufficient to detach the material from the nozzle. For the same driving voltage, slight variations in droplet velocity across the nozzles of about ±0.5 m/s are typical and might have contributed to the observed deviation in Fig. 16a. Moreover, the measurement of the bubble surface at short surface age (high frequencies) is particularly challenging and prone to error [73]. For example, severe foaming occurred during the measurement of M2 at short surface age which reduced the accuracy of the results as well.

In Fig. 16b, the model curve for material M3 at 26 °C predicts the velocity accurately. Only very small deviations of less than 8 % are observed for higher driving voltages. However, the modelled curve for 45 °C underperforms significantly and demonstrates larger deviation of around -3 m/s throughout all temperatures. Source of such large errors could be inaccuracies of the applied model for estimating the values at extreme dynamic range, at higher temperatures, or by an inaccurate regression model based on linear combination.

Surface tension is the main driving force for satellite droplet formation. The Hua & Rosen model utilized for predicting the surface tension at extreme dynamic range might be inaccurate as it is an empirical model calibrated for water-based solution with surfactant. Due to the higher viscosity of the UV-inks and the presence of polymer with long molecule chains, the diffusion of surfactant is expected to be slower compared to their diffusion in water. This means that the surface age at 0 ms predicted with Hua & Rosen model is most likely higher than the actual value. Furthermore, determining the coefficients of the Eötvös model requires the composition of the ink to be known to obtain information about molecular volume and critical temperature. Commercial ink formulations are typically not fully disclosed, therefore the estimated surface tensions at various temperature are also subject to uncertainty. However, it is to be noted that the surface tension component in the regression model mainly influences the slope and does not explain such large deviation.

With regards to complex viscosity, Cross model couldn't be successfully applied to the measurement result of M3, because it yielded an unreasonable low viscosity at high frequency rate. This result suggests that Cross model might estimate viscosities at high frequencies with limited accuracy. The work-around of calculating the high frequency viscosity by applying an average shear-thinning ratio yielded reasonable values, but could also introduce further errors since the shear-thinning behavior is influenced by the ink's composition.

An attempt is made to optimize the modelled curve for M3. By introducing a correction factor of 3 to the density and 2.4 to the storage modulus scalar coefficients, a much closer fit to the experimental data at higher temperatures could be achieved. This improvement points at a higher contribution of inertia and storage modulus to the droplet velocity/voltage curve and suggest a non-linear combination of the rheological properties. The plot after optimization and the applied correction factors can be found in the Appendix.

The validation results show that the derived model, which correlates driving voltage with droplet velocity, provides substantial support in narrowing the range of driving voltages for which a stable single droplet jetting can be expected. While the model exhibits some variability, it provides valuable guidance, and a jetting condition with an estimated droplet velocity of around 2.8 m/s is recommended as a practical starting point. This approach can lead to a first-time-right set of jetting parameters for a stable single droplet. If one satellite droplet at this condition is visible, further optimization of the driving voltage by no more than 5 % is sufficient to establish a stable single droplet jetting condition.

5. Conclusion and outlook

The objective of this study was to develop an efficient yet affordable methodology for UV-curable polymer inkjet inks that determines both their printability and the unipolar waveform parameters needed to generate satellite-free droplets with a piezo-driven industrial printhead. The work synthesizes the findings of three key aspects: Firstly, the findings regarding the relevant rheological properties for causing satellite droplets in inkjet printing. Secondly, the relationship between droplet velocity and the parameters of a bipolar waveform, namely pulse width and driving voltage. Thirdly, how variation of rheological properties affects the droplet velocity.

The study was carried out with two commercially available 3D-printing inkjet inks. These materials were characterised at multiple temperatures for complex viscosity, viscoelasticity (storage and loss moduli), density, dynamic surface tension, and oscillation-/damping behaviour. Meanwhile, dropwatching, droplet volume verification and print stability tests were also conducted to obtain information about the actual jetting behaviour.

Based on these examinations, following conclusions can be made:

- Rheological properties alone do not fully determine the number of satellite droplets. Despite the ink's rheological properties being the same, the droplet behaviour changes with modification of the waveform parameters.

- The extreme dynamic range in inkjet printing requires constitutive and empirical models to be applied to the measurement results of the rheological properties, namely Cross model for complex viscosity, Hua & Rosen model for dynamic surface tension and Maxwell model for Loss and Storage modulus.
- Arrhenius and Eötvös models are utilized to predict the complex viscosity and surface tension for other jetting temperatures. For the other material properties density, relaxation number and storage modulus a linear fit is applied. These three physical properties decrease in a linear manner with increasing temperature.
- It has been observed for all jetted materials that droplets with velocity between 2 and 3 m/s are stable and free of satellite droplets. Droplet velocity seems to be a stable criterion across all materials for estimating the number of satellite droplets.
- Droplet velocity is linearly correlated to driving voltage, and a parabolic correlation between droplet velocity and pulse width is observed.
- Optimal pulse width can be estimated using the piezo oscillation measurement, assuming that the relaxation time is shorter than the estimated pulse width. Otherwise, the relaxation time governs the optimal pulse width.
- The slope and y-intersect values of the linear equation describing the interdependence between droplet velocity and driving voltage are defined by the four key rheological material properties, namely complex viscosity, surface tension, storage modulus and density.
- A regression model is established based a linear combination of the four relevant rheological properties complex viscosity, surface tension, storage modulus and density. The rheological parameters are first to be modelled for the high dynamic range at different jetting temperature. By inserting the modelled rheological parameters into the resulting linear regression equation, the slope and y-intersect coefficients of the driving voltage/droplet velocity curve can be determined.
- A validation of the methodology and the model is performed with two inks at various jetting condition. The validation confirms that the proposed approach for determining the printable zone by utilizing the droplet velocity/driving voltage curve and a stable droplet velocity zone around 2.8 m/s can estimate the stable droplet printing area. This approach can limit the search area for driving voltage considerably (down to ±5 %). However, at high temperatures, the deviation between the actual and predicted droplet velocity becomes larger.

This methodology allows a potential driving voltage range and the pulse width to be determined based on few rheological measurements, so that a suitable unipolar waveform can be derived directly for commercial polymer inks.

In future studies, more inks, and in particular inks of different types, such as particle-loaded ones, will be examined, to further refine the methodology. The derived model correlating velocity and driving voltage at various temperatures are to be tested on other printhead types as well. Furthermore, more accurate models for estimating the rheological properties in extreme dynamic range are required. Deploying a non-linear combination for the regression model can enhance the accuracy of model. Automation of dropwatching and rheological measurements can increase the number of data collected which is beneficial to further advance the methodology.

6. Authors agreement

We the undersigned declare that this manuscript (manuscript ID: JMADE-D-25-03040, entitled “Satellite Free Droplet Formation in Material Jetting via Rheology Driven Waveform Modelling Approach”) is original, has not been published before and is not currently being considered for publication elsewhere.

We confirm that the manuscript has been read and approved by all named authors and that there are no other persons who satisfied the criteria for authorship but are not listed. We further confirm that the order of authors listed in the manuscript has been approved by all of us.

We understand that the Corresponding Author is the sole contact for the Editorial process. She is responsible for communicating with the other authors about progress, submissions of revisions and final approval of proofs.

CRediT authorship contribution statement

Karin J. Chen: Writing – review & editing, Writing – original draft, Visualization, Validation, Methodology, Investigation, Formal analysis, Data curation, Conceptualization. **Veit Hagenmeyer:** Writing – review & editing, Supervision, Funding acquisition. **Ahmed Elkaseer:** Writing – review & editing, Methodology, Formal analysis, Data curation.

Funding

This work was carried out with the financial support of the Karlsruhe Nano Micro Facility (KNMFi, www.knmf.kit.edu), a Helmholtz Research Infrastructure at Karlsruhe Institute of Technology (KIT, www.kit.edu) and under the Helmholtz Research Programme MSE (Materials Systems Engineering) at KIT.

Declaration of competing interest

The authors declare that they have no known competing financial interests or personal relationships that could have appeared to influence the work reported in this paper.

Acknowledgement

The authors would like to thank Dr. Steffen Scholz from KIT for the insightful discussions that inspired this study. We also acknowledge the support provided by the KIT-Publication Fund of the Karlsruhe Institute of Technology.

Appendix A. Supplementary data

Supplementary data to this article can be found online at https://doi.org/10.1016/j.matdes.2025.115252.

Data availability

Data will be made available on request.

References

[1] P. Zhao, et al., Modelling the influence of UV curing strategies for optimisation of inkjet based 3D printing, Mater. Des. 208 (2021) 109889, https://doi.org/10.1016/j.matdes.2021.109889.
[2] S. Kriegseis, L. Aretz, M.-E. Jennes, F. Schmidt, T. Tonnesen, K. Schickle, 3D printing of complex ceramic dental implant abutments by using Direct Inkjet Printing, Mater. Lett. 313 (2022) 131789, https://doi.org/10.1016/j.matlet.2022.131789.
[3] L.A. Ruiz-Preciado, P. Pesek, C. Guerra-Yanez, Z. Ghassemlooy, S. Zvanovec, G. Hernandez-Sosa, Inkjet-printed high-performance and mechanically flexible organic photodiodes for optical wireless communication, Sci. Rep. 14 (1) (2024) 3296, https://doi.org/10.1038/s41598-024-53796-5.
[4] L.B. Bezek, C.A. Chatham, D.A. Dillard, C.B. Williams, Mechanical properties of tissue-mimicking composites formed by material jetting additive manufacturing, (in eng), J. Mech. Behav. Biomed. Mater. 125 (2022) 104938, https://doi.org/10.1016/j.jmbbm.2021.104938.
[5] J.D. Hubbard, et al., Fully 3D-printed soft robots with integrated fluidic circuitry, Sci. Adv. 7 (29) (2021), https://doi.org/10.1126/sciadv.abe5257.
[6] O. Song, et al., All inkjet-printed electronics based on electrochemically exfoliated two-dimensional metal, semiconductor, and dielectric, NPJ 2D Mater. Appl. 6 (1) (2022) 64, https://doi.org/10.1038/s41699-022-00337-1.
[7] T.N. Mangoma, S. Yamamoto, G.G. Malliaras, R. Daly, Hybrid 3D/Inkjet-printed organic neuromorphic transistors, Adv. Mater. Technol. 7 (2) (2022) 2000798, https://doi.org/10.1002/admt.202000798.

[8] Q. Jin, et al., Inkjet-printed optical interference filters, Nat. Commun. 15 (1) (2024) 3372, https://doi.org/10.1038/s41467-024-47086-x.
[9] I. Marasco, et al., A compact evolved antenna for 5G communications, (in eng), Sci. Rep. 12 (1) (2022) 10327, https://doi.org/10.1038/s41598-022-14447-9.
[10] C. McIlroy, O.G. Harlen, N.F. Morrison, Modelling the jetting of dilute polymer solutions in drop-on-demand inkjet printing, J. Nonnewton. Fluid Mech. 201 (2013) 17–28, https://doi.org/10.1016/j.jnnfm.2013.05.007.
[11] H. Yoo, C. Kim, Generation of inkjet droplet of non-Newtonian fluid, Rheol. Acta 52 (4) (2013) 313–325, https://doi.org/10.1007/s00397-013-0688-4.
[12] S.D. Hoath, et al., Oscillations of aqueous PEDOT:PSS fluid droplets and the properties of complex fluids in drop-on-demand inkjet printing, J. Nonnewton. Fluid Mech. 223 (2015) 28–36, https://doi.org/10.1016/j.jnnfm.2015.05.006.
[13] J.S.R. Wheeler, S.G. Yeates, Polymers in Inkjet Printing, Fund. Inkjet Print. (2016) 117–140.
[14] C. Clasen, P.M. Phillips, L. Palangetic, A.J. Vermant, Dispensing of rheologically complex fluids: the map of misery, AIChE J 58 (10) (2011) 3242–3255, https://doi.org/10.1002/aic.13704.
[15] I.M. Hutchings, G.D. Martin, S.D. Hoath, Introductory Remarks, Fund. Inkjet Print. (2016) 1–12.
[16] T.D. Grant, et al., Inkjet printing of high-concentration particle-free platinum inks, Mater. Des. 214 (2022), https://doi.org/10.1016/j.matdes.2021.110377.
[17] X. Jiang, et al., Enhanced morphology and conductivity in aerosol jet printing via optimization of print speed range under various deposition rate, Mater. Des. 259 (2025), https://doi.org/10.1016/j.matdes.2025.114745.
[18] S. Fathi, P. Dickens, R. Hague, Instability behaviours of a jet array in inkjet printing of molten caprolactam, Rapid Prototyp. J. 19 (3) (2013) 189–198, https://doi.org/10.1108/13552541311312184.
[19] H. Wijshoff, Structure and fluid-dynamics in piezo inkjet printheads, Doctor of Philosophy, Oce Technologies, University Twente, Venlo, 2008. [Online]. https://ris.utwente.nl/ws/portalfiles/portal/6085963/thesis_Wijshoff.pdf.
[20] L. Rayleigh, On the Instability of jets, Proc. Lond. Math. Soc. s1–10 (1) (1878) 4–13, https://doi.org/10.1112/plms/s1-10.1.4.
[21] O. Breslouer, Rayleigh-Plateau Instability: Falling Jet, Princeton University, 2010. Accessed: 06.10.2025. [Online]. Available: https://www.princeton.edu/~stonelab/Teaching/Oren%20Breslouer%20559%20Final%20Report.pdf.
[22] H. Khodayari, F. Ommi, Z. Saboohi, Investigation of the primary breakup length and instability of non-Newtonian viscoelastic liquid jets, Int. J. Multiphys. 12 (4) (2018). https://doi.org/10.21152/1750-9548.12.4.327.
[23] A. Javadi, J. Eggers, D. Bonn, M. Habibi, N.M. Ribe, Delayed capillary breakup of falling viscous jets, Phys. Rev. Lett. 110 (14) (2013), https://doi.org/10.1103/PhysRevLett.110.144501.
[24] Y. Christanti, L.M. Walker, Effect of fluid relaxation time of dilute polymer solutions on jet breakup due to a forced disturbance, J. Rheol. 46 (3) (2002) 733–748, https://doi.org/10.1122/1.1463418.
[25] D. Jang, D. Kim, J. Moon, Influence of fluid physical properties on ink-jet printability, (in eng), Langmuir: ACS J. Surf. Colloids 25 (5) (2009) 2629–2635, https://doi.org/10.1021/la900059m.
[26] S. Jung, H.J. Hwang, S.H. Hong, Drops on substrates, Fund. Inkjet Print. (2016) 199–218.
[27] S. Kim, M. Cho, S. Jung, The design of an inkjet drive waveform using machine learning, Sci. Rep. 12 (1) (2022) 4841, https://doi.org/10.1038/s41598-022-08784-y.
[28] W. Jianjun, et al., Actuation waveform auto-design of drop-on-demand inkjet for ejection droplet without satellite, J. Manuf. Process. 102 (2023) 910–920, https://doi.org/10.1016/j.jmapro.2023.08.021.
[29] Y. Zhong, H. Fang, Q. Ma, X. Dong, Analysis of droplet stability after ejection from an inkjet nozzle, J. Fluid Mech. 845 (2018) 378–391, https://doi.org/10.1017/jfm.2018.251.
[30] S.D. Hoath, et al., Inkjet printing of weakly elastic polymer solutions, J. Nonnewton. Fluid Mech. 205 (2014) 1–10, https://doi.org/10.1016/j.jnnfm.2014.01.002.
[31] S. Hoath, W. K. Hsiao, S. Jung, G. Martin, and I. Hutchings, Dependence of Drop Speed on Nozzle Diameter, Viscosity and Drive Amplitude in Drop-on-Demand Ink-Jet Printing. 2011.
[32] P. Duineveld *et al.*, Ink-jet printing of polymer light-emitting devices, Presented at the International Symposium on Optical Science and Technology, San Diego, CA, United States, 27 February 2002, 2002, OP. [Online]. Available: https://doi.org/10.1117/12.457460.
[33] A.H. Hamad, M.I. Salman, A. Mian, Effect of driving waveform on size and velocity of generated droplets of nanosilver ink (Smartink), Manuf. Lett. 24 (2020) 14–18, https://doi.org/10.1016/j.mfglet.2020.03.001.
[34] S. Seipel, J. Yu, V.A. Nierstrasz, Effect of physical parameters and temperature on the piezo-electric jetting behaviour of UV-curable photochromic inks, Sci. Rep. 10 (1) (2020) 18841, https://doi.org/10.1038/s41598-020-75449-z.
[35] Y. Liu, B. Derby, Experimental study of the parameters for stable drop-on-demand inkjet performance, *Phys. Fluids* 31(3) (2019), doi: 10.1063/1.5085868.
[36] N.F. Morrison, O.G. Harlen, Viscoelasticity in inkjet printing, Rheol. Acta 49 (6) (2010) 619–632, https://doi.org/10.1007/s00397-009-0419-z.
[37] T. Tuladhar, R. Harvey, J. Tatum, P. Drury, Understanding inkjet inks and factors influencing the jetting behaviour, NIP & Digit. Fabr. Conf. 25 (1) (2009) 423–426, https://doi.org/10.2352/ISSN.2169-4451.2009.25.1.art00004_2.
[38] U. Sen, et al., The retraction of jetted slender viscoelastic liquid filaments, J. Fluid Mech. 929 (2021), https://doi.org/10.1017/jfm.2021.855.
[39] B. Derby, Inkjet printing of functional and structural materials: fluid property requirements, feature stability, and resolution, Annu. Rev. Mat. Res. 40 (1) (2010) 395–414, https://doi.org/10.1146/annurev-matsci-070909-104502.
[40] B. Derby, Additive manufacture of ceramics components by inkjet printing, Engineering 1 (1) (2015) 113–123, https://doi.org/10.15302/j-eng-2015014.
[41] Z. Du, et al., Controlling the polymer ink's rheological properties to form single and stable droplet, Coatings 14 (5) (2024), https://doi.org/10.3390/coatings14050600.
[42] G.H. McKinley, M. Renardy, Wolfgang von Ohnesorge, Phys. Fluids 23 (12) (2011), https://doi.org/10.1063/1.3663616.
[43] D. Lohse, Fundamental Fluid Dynamics challenges in Inkjet Printing, Annu. Rev. Fluid Mech. 54 (1) (2022) 349–382, https://doi.org/10.1146/annurev-fluid-022321-114001.
[44] E. Kim, J. Baek, Numerical study on the effects of non-dimensional parameters on drop-on-demand droplet formation dynamics and printability range in the up-scaled model, *Phys. Fluids* 24(8) (2012), doi: 10.1063/1.4742913.
[45] H.C. Nallan, J.A. Sadie, R. Kitsomboonloha, S.K. Volkman, V. Subramanian, Systematic design of jettable nanoparticle-based inkjet inks: rheology, acoustics, and jettability, Langmuir 30 (44) (2014) 13470–13477, https://doi.org/10.1021/la502903y.
[46] E. García-Tuñón, R. Agrawal, B. Ling, D.J.C. Dennis, Fourier-transform rheology and printability maps of complex fluids for three-dimensional printing, *Phys. Fluids* 35(1) (2023), doi: 10.1063/5.0128658.
[47] Z. Du, Y. Lin, R. Xing, X. Cao, X. Yu, Y. Han, Controlling the polymer ink's rheological properties and viscoelasticity to suppress satellite droplets, Polymer 138 (2018) 75–82, https://doi.org/10.1016/j.polymer.2018.01.052.
[48] S. Kim, R. Wenger, O. Bürgy, G. Balestra, U. Jeong, S. Jung, Predicting inkjet jetting behavior for viscoelastic inks using machine learning, *Flex. Print. Electron.* 8(3) (2023), doi: 10.1088/2058-8585/acee94.
[49] P. Suly, J. Sevcik, D.J. Dmonte, P. Urbanek, I. Kuritka, Inkjet printability assessment of weakly viscoelastic fluid: a semidilute polyvinylpyrrolidone solution ink case study, Langmuir 37 (28) (2021) 8557–8568, https://doi.org/10.1021/acs.langmuir.1c01010.
[50] J. M. Richardot, S. Kim, S. Jung, Evaluating inkjet printability of viscoelastic ink through Deborah number analysis, *Phys. Fluids* 37(2) (2025), doi: 10.1063/5.0253639.
[51] J. Tai, H. Gan, Y. Liang, B. Lok, Control of droplet formation in inkjet printing using ohnesorge number category: materials and processes, in: *10th Electronics Packaging Technology Conference, EPTC 2008,* 12/01 2008, doi: 10.1109/EPTC.2008.4763524.
[52] J.-M. Lai and J.-D. Lin, Numerical investigation of the effect of the transducer pulse on the drop ejection process, in: *2009 IEEE 3rd International Conference on Nano/Molecular Medicine and Engineering*, 18-21 Oct. 2009 2009, pp. 221–226, doi: 10.1109/NANOMED.2009.5559083.
[53] H. Ramli, N.F.A. Zainal, M. Hess, C.H. Chan, Basic principle and good practices of rheology for polymers for teachers and beginners, Chem. Teacher Int. 4 (4) (2022) 307–326, https://doi.org/10.1515/cti-2022-0010.
[54] S.D. Hoath, I.M. Hutchings, G.D. Martin, T.R. Tuladhar, M.R. Mackley, D. Vadillo, Links between ink rheology, drop-on-demand jet formation, and printability, J. Imaging Sci. Technol. 53 (4) (2009) 041208, https://doi.org/10.2352/J.ImagingSci.Technol.2009.53.4.041208.
[55] L. Kirschenmann, W. Pechhold, Piezoelectric Rotary Vibrator (PRV) – a new oscillating rheometer for linear viscoelasticity, Rheol. Acta 41 (4) (2002) 362–368, https://doi.org/10.1007/s00397-002-0229-z.
[56] J.J. Crassous, R. Régisser, M. Ballauff, N. Willenbacher, Characterization of the viscoelastic behavior of complex fluids using the piezoelastic axial vibrator, J. Rheol. 49 (4) (2005) 851–863, https://doi.org/10.1122/1.1917843.
[57] N. Godard, M.A. Mahjoub, S. Girod, T. Schenk, S. Glinšek, E. Defay, On the importance of pyrolysis for inkjet-printed oxide piezoelectric thin films, J. Mater. Chem. C 8 (11) (2020) 3740–3747, https://doi.org/10.1039/c9tc05228c.
[58] S. Majee *et al.*, Low temperature chemical sintering of inkjet-printed Zn nanoparticles for highly conductive flexible electronic components, *NPJ Flex. Electron.* 5(1) (2021), doi: 10.1038/s41528-021-00111-1.
[59] A.V. Bazilevskii, J.D. Meyer, A.N. Rozhkov, Dynamics and breakup of pulse microjets of polymeric liquids, Fluid Dyn. 40 (3) (2005) 376–392, https://doi.org/10.1007/s10697-005-0078-4.
[60] D. Zhao, H. Zhou, Y. Wang, J. Yin, Y. Huang, Drop-on-demand (DOD) inkjet dynamics of printing viscoelastic conductive ink, Addit. Manuf. 48 (2021), https://doi.org/10.1016/j.addma.2021.102451.
[61] A. Götz, J.C. Janhsen, S. Güttler, O. Refle, O. Ronczka, A systematic approach to evaluate jetability of high-viscosity resins for 3D inkjet printing applications, Prog. Addit. Manuf. 10 (3) (2025) 1707–1712, https://doi.org/10.1007/s40964-025-00958-0.
[62] A. Paar, U-tube technology in digital laboratory density meters. https://wiki.anton-paar.com/de-de/digitale-labor-dichtemessgeraete-mit-biegeschwinger-technologie/ (Accessed 26 Feb, 2025).
[63] Y.H. Shim, J.J. Griebler, S.A. Rogers, A reexamination of the Cox–Merz rule through the lens of recovery rheology, J. Rheol. 68 (3) (2024) 381–396, https://doi.org/10.1122/8.0000811.
[64] G.S. Manning, On the thermodynamic stability of bubbles, immiscible droplets, and cavities, Phys. Chem. Chem. Phys. 22 (31) (2020) 17523–17531, https://doi.org/10.1039/d0cp02517h.
[65] V.B. Fainerman, R. Miller, P. Joos, The measurement of dynamic surface tension by the maximum bubble pressure method, Colloid Polym. Sci. 272 (6) (1994) 731–739, https://doi.org/10.1007/bf00659287.
[66] S.C. Hauswirth, et al., Modeling cross model non-Newtonian fluid flow in porous media, J. Contam. Hydrol. 235 (Nov 2020) 103708, https://doi.org/10.1016/j.jconhyd.2020.103708.

[67] J.C. Weddell, J. Kwack, P.I. Imoukhuede, A. Masud, Hemodynamic analysis in an idealized artery tree: differences in wall shear stress between Newtonian and non-Newtonian blood models, PLoS One 10 (4) (2015) e0124575, https://doi.org/10.1371/journal.pone.0124575.
[68] F.J. Stadler, T. Mahmoudi, Understanding the effect of short-chain branches by analyzing viscosity functions of linear and short-chain branched polyethylenes, Korea-Austral. Rheol. J. 23 (4) (2012) 185–193, https://doi.org/10.1007/s13367-011-0023-5.
[69] M. Peleg, Temperature-viscosity models reassessed, Crit. Rev. Food Sci. Nutr. 58 (15) (2018) 2663–2672, https://doi.org/10.1080/10408398.2017.1325836.
[70] X.Y. Hua, M.J. Rosen, Dynamic surface tension of aqueous surfactant solutions, J. Colloid Interface Sci. 124 (2) (1988) 652–659, https://doi.org/10.1016/0021-9797(88)90203-2.
[71] L. Zhang, Y. Zhu, X. Cheng, C. Wang, The simulation study of fluid physical properties on drop formation of drop-on-demand inkjet printing, MATEC Web Conf. 25 (2015), https://doi.org/10.1051/matecconf/20152503011.
[72] P. C. Duineveld *et al.*, Ink-jet printing of polymer light-emitting devices, in: *Organic Light-Emitting Materials and Devices V*, Z. H. Kafafi Ed., (SPIE Proceedings: SPIE, 2001, p. 59.
[73] SINTERFACE Technologies, Bubble Pressure Analyser BPA-1P, Max Planck Institute of Colloids and Interfaces. [Online]. https://www.mpikg.mpg.de/4862784/BPA-1P-Info.pdf.